AEDC-TR-73-102

Cy 2

AN ANALYTICAL INVESTIGATION OF VISCOUS SHOCK-LAYER FLOW NEAR THE LEADING EDGE OF SLENDER BODIES UNDER LOW-DENSITY HYPERSONIC CONDITIONS

J. R. Maus

ARO, Inc.

June 1973

VON KÁRMÁN GAS DYNAMICS FACILITY
ARNOLD ENGINEERING DEVELOPMENT CENTER
AIR FORCE SYSTEMS COMMAND
ARNOLD AIR FORCE STATION, TENNESSEE

NOTICES

When U. S. Government drawings specifications, or other data are used for any purpose other than a definitely related Government procurement operation, the Government thereby incurs no responsibility nor any obligation whatsoever, and the fact that the Government may have formulated, furnished, or in any way supplied the said drawings, specifications, or other data, is not to be regarded by implication or otherwise, or in any manner licensing the holder or any other person or corporation, or conveying any rights or permission to manufacture, use, or sell any patented invention that may in any way be related thereto.

Qualified users may obtain copies of this report from the Defense Documentation Center.

References to named commercial products in this report are not to be considered in any sense as an endorsement of the product by the United States Air Force or the Government.

AN ANALYTICAL INVESTIGATION OF VISCOUS SHOCK-LAYER FLOW NEAR THE LEADING EDGE OF SLENDER BODIES UNDER LOW-DENSITY HYPERSONIC CONDITIONS

by

J. R. Maus*

*Consultant to ARO, Inc., and Associate Professor of Aerospace Engineering, The University of Tennessee Space Institute.

FOREWORD

The work reported herein was conducted by the Arnold Engineering Development Center (AEDC), Air Force Systems Command (AFSC), under Program Element 65802F.

The results of research presented were obtained by ARO, Inc. (a subsidiary of Sverdrup & Parcel and Associates, Inc.), contract operator of AEDC, AFSC, Arnold Air Force Station, Tennessee. The work was conducted from July 1969 to July 1972 by Dr. J. R. Maus under AEDC Research Project No. VW5006 and the ARO, Inc.-UTSI Services Subcontract. The manuscript was submitted for publication on March 8, 1973.

The initial analysis and computer program development were performed by Dr. J. C. Adams, Jr. and Mr. G. E. Gilley, ARO, Inc., von Kármán Gas Dynamics Facility. The author wishes to express his appreciation to these individuals for their assistance in this work.

This technical report has been reviewed and is approved.

ELTON R. THOMPSON
Research and Development Division
Directorate of Technology

ROBERT O. DIETZ
Director of Technology

ABSTRACT

An analytical investigation and a numerical procedure are presented for calculating the fully viscous shock-layer flow near the sharp leading edge of both two-dimensional and axisymmetric slender bodies under hypersonic low-density flow conditions. The calculation method is based on numerical integration of the governing continuum fluid mechanical equations of motion using an implicit finite-difference technique in conjunction with wall slip boundary conditions; the shock structure is determined as part of the resulting solution. The mathematical model used in the present investigation represents a considerable improvement over previously published continuum studies in that a more complete and accurate set of governing equations and boundary conditions is employed. The results of the numerical calculations have been compared with previous flat-plate test results taken in the von Kármán Facility Low Density Hypersonic Wind Tunnel (L) by Becker and Boylan; in general, good to excellent agreement between the present theory and experiment is revealed.

CONTENTS

ILLUSTRATIONS

Figure | Page

NOMENCLATURE

A_n, B_n, C_n, D_n	Coefficients in finite-difference equations, Eq. (39)
a	Local speed of sound
C	Chapman-Rubesen constant, $(\mu_w T_\infty)/(\mu_\infty T_w)$
C_f	Skin-friction coefficient, $\tau_w/(1/2\ \bar{\rho}_\infty)\bar{U}_\infty$
C_H	Stanton Number, $\dot{q}/\bar{\rho}_\infty \bar{U}_\infty \bar{c}_p (\bar{T}_o - \bar{T}_\infty)$
E_n, F_n	Coefficients in inversion formulas, Eq. (44)
h	Static enthalpy
$\bar{k}$	Thermal conductivity
$\bar{L}$	Characteristic length, 1 in. in all calculations
$\bar{\ell}$	Molecular mean free path
M_∞	Mach number, $\bar{U}_\infty/\sqrt{\gamma \bar{R} \bar{T}_\infty}$
N	Total number of grid points
Pr	Prandtl number, $c_p \mu/k$
p	Static pressure
p_o	Pitot pressure
$\dot{q}$	Heat flux
$\bar{R}$	Gas constant
Re	Reynolds number $\rho_\infty U_\infty L/\mu_\infty$
Re_x	Reynolds number $\rho_\infty U_\infty x/\mu_\infty$
r	Radius in cylindrical coordinates
r_o	Local radius of cone
T	Static temperature
T_o	Stagnation temperature
U_∞	Free-stream velocity
u	x-component of velocity

$\overline{V}_{x,\infty}$	Hypersonic interaction parameter, $M_\infty \sqrt{C}/\sqrt{Re_x}$
v	y-component of velocity
w	General dependent variable
x	Coordinate along the body
y	Coordinate normal to the body
α	Thermal accommodation coefficient
$\alpha_1, \alpha_2, \alpha_3, \alpha_4$	Coefficients in "standard" parabolic differential equation
γ	Ratio of specific heats
η	Transformed normal coordinate, Eq. (18)
θ	Angle of attack
θ_c	Cone half angle
μ	Dynamic viscosity
μ_B	Bulk viscosity
ξ	Transformed independent variable
π	Pi, 3.14159
ρ	Density
σ	Accommodation coefficient for momentum
$\overline{\chi}$	Hypersonic parameter, $M_\infty^3 \sqrt{C}/\sqrt{Re_x}$
$(\overline{\ })$	Denotes dimensional quantities
$(\ )_\infty$	Denotes free-stream conditions

SECTION I
INTRODUCTION

1.1 BACKGROUND

Rarefied hypersonic flow over slender bodies having sharp leading edges has been a problem of considerable interest for a number of years. A great deal of both experimental and theoretical work has been done on flows of this type; in particular, the hypersonic flow over a flat plate has received much attention. From these studies a fairly definite qualitative description of the flow field has emerged. A schematic showing the essential features of hypersonic flow over a flat plate is presented in Fig. 1. It is well known that the viscous retardation of the flow near the plate surface deflects the outer streamlines and generates a shock wave. The so-called merged layer begins where the molecular mean free path is small enough compared to the thickness of the disturbed layer that the equations of continuum fluid mechanics are applicable. Upstream of the merged layer, near the leading edge, a noncontinuum approach is required. In the merged layer, the shocklike structure is still diffuse and cannot be treated separately from the viscous region. At the surface of the plate there is relative slip motion between the plate and the fluid and a temperature jump across this interface. As the flow proceeds downstream, the compression region merges into a Rankine-Hugoniot shock, and a distinct inviscid region develops between the shock wave and the viscous boundary layer. This region is known as the strong interaction regime, where the classical boundary-layer equations are applicable, but the development of the viscous flow region and the inviscid flow are still strongly interdependent. Further downstream the self-induced shock wave weakens and the inviscid flow is essentially a perturbation of the undisturbed flow conditions. In this weak interaction region classical Prandtl boundary-layer theory, coupled to the inviscid flow by the displacement effect, can be applied.

The present study is concerned with hypersonic flow in the merged layer regime, where a continuum analysis is applicable but the Prandtl boundary-layer equations are inadequate to properly describe the flow. In this report a calculation procedure for two-dimensional hypersonic flow over flat plates and wedges and axisymmetric flow past circular cones is presented.

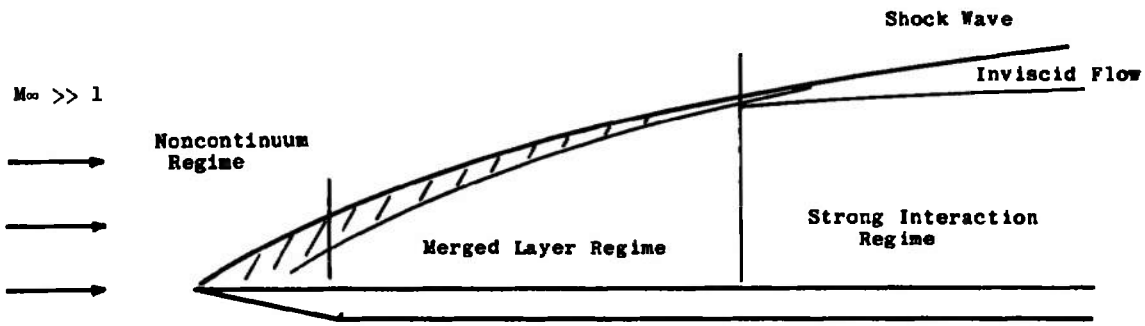

Fig. 1 Viscous Hypersonic Flow Field for Flat Plate

1.2 PREVIOUS ANALYTICAL STUDIES

One of the first efforts to analyze the merged layer over a flat plate was carried out by Pan and Probstein (Ref. 1). The mathematical model employed the usual compressible boundary-layer equations augmented by the inviscid y-momentum equation to describe the transverse pressure variations. These equations were reduced to ordinary differential equations by a local similarity approximation. Velocity slip and temperature jump boundary conditions were applied at the plate surface. Taking into account shock thickness and curvature, modified Rankine-Hugoniot conditions were derived for the tangential component of velocity and temperature behind the shock. These conditions were used as the outer boundary conditions for the merged layer.

Shorenstein and Probstein (Ref. 2), following the work of Oguchi (Ref. 3), extended the analysis of Pan and Probstein to take into account the departure of normal velocity component and density from the Rankine-Hugoniot values. Shorenstein and Probstein used the same set of simplified equations as Pan and Probstein to describe the flow in the merged layer. The results of both of these studies showed good qualitative agreement between the data compared. The quantitative agreement generally improved as the effects of shock curvature and wall slip were included in the calculations.

Chow (Ref. 4) divided the merged layer into two subregions, a shock wavelike region and a boundary-layerlike region, requiring that the velocity and the velocity gradient be continuous along their common boundary. An integral analysis was applied to the merged layer, assuming a cubic velocity profile with slip in the boundary-layer region. The Crocco relationship was used to express temperature in terms of

velocity and thereby eliminate the energy equation. Comparison of the results of the calculations with experimental data showed reasonably good agreement.

In a series of reports and publications (Refs. 5, 6, and 7) Rubin and his colleages have documented a calculation method that is very similar to that of the present study and indeed have provided the incentive for this work. In the initial publication in the open literature, Rudman and Rubin (Ref. 6) reduced the governing conservation equations to a form applicable to the entire disturbed flow region for a two-dimensional flat plate. The equations used were essentially two-dimensional boundary-layer equations ignoring the longitudinal pressure gradient $\partial p/\partial x$ but augmented by the lateral momentum equation to account for the transverse pressure gradient. These equations were integrated step by step, using an explicit finite-difference technique through the entire disturbed layer including the shocklike structure. The results of these calculations agree fairly well with experimental pressure and heat-transfer data although the profiles exhibited an unusual behavior in the shock wave region as the strong interaction region was approached. This was initially thought by Rudman and Rubin to be a weak compression wave behind the shock but was later found to be a result of an inadequate description of the shock structure. In a succeeding publication, the theory was extended to axisymmetric cones and simple three-dimensional flows (Ref. 7).

Cheng et al. (Ref. 8) developed a calculation procedure very similar to that of Rudman and Rubin for application to the merged layer for a flat plate. The equation set used was somewhat different from that of Ref. 5, however; in particular, the longitudinal pressure gradient term was included in the x-momentum equation. Inclusion of this term can produce a singularity in the equations at the sonic point $u = a$. This singularity is discussed in some detail by Cheng et al. and by Token (Ref. 9), who used a similar equation set to calculate viscous hypersonic flow in slender axisymmetric nozzles. The profiles obtained by Cheng et al., like those of Rudman and Rubin, exhibited a kink in the outer portion as the shock structure became thin. It was reported that this kink disappeared as the grid and step sizes of the calculation procedure were reduced.

Recently Kot and Turcotte (Ref. 10) presented an interesting study on flow over a flat plate in which the hypersonic free stream is modeled by a zero-temperature molecular beam. By collision with continuum molecules, these beam molecules are themselves converted to continuum

molecules. The beam molecules are assumed to have a delta-function velocity distribution and the continuum molecules a near-Maxwellian distribution. Kot and Turcotte developed partial differential equations describing the interaction of the beam molecules and the continuum fluid and integrated these equations using a finite-difference scheme. The results of their calculations, however, appear to be very similar to pure continuum approaches such as those used in this study.

SECTION II
MATHEMATICAL MODEL

2.1 GOVERNING EQUATIONS

The mathematical formulation will first be presented for two-dimensional hypersonic flow over flat plates. The geometry and coordinate system under consideration for this case are shown in Fig. 2.

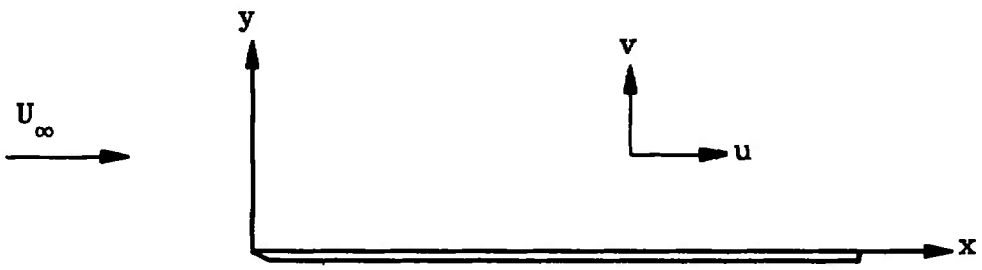

a. Zero Angle of Attack

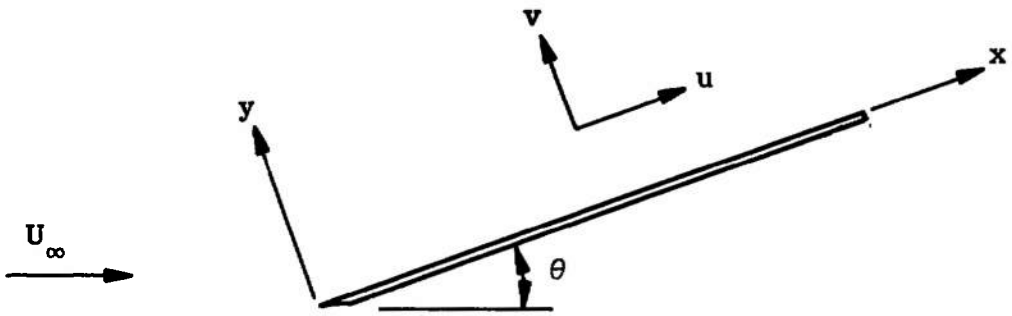

b. Nonzero Angle of Attack

Fig. 2 Geometry and Coordinates for Two-Dimensional Flow

The equations describing such a flow field are the steady, two-dimensional compressible conservation equations for mass, momentum, and energy as given in Ref. 11. Since a forward-marching method of solution, such as is used for laminar boundary layers, was planned, the equations were parabolicized by deleting second-derivative terms in the streamwise (x) direction. From previous analyses (Refs. 5 and 8), it is well known that for thin, viscous shock layers, terms of the form $\frac{\partial}{\partial \bar{x}}\left(\bar{k}\,\frac{\partial \overline{w}}{\partial \bar{x}}\right)$ are negligible, compared to other terms of the equations. It should be pointed out that under the thin shock-layer assumption there are in the conservation equations additional terms which are of the same order as these terms and which could be justifiably dropped on an order-of-magnitude basis (Ref. 5). However, since the additional terms could be handled by the technique used to solve the equations, it was considered worth the slight extra programming effort and machine time required to retain them. With the terms $\frac{\partial}{\partial \bar{x}}\left(\bar{\mu}\,\frac{\partial \overline{w}}{\partial x}\right)$ and $\frac{\partial}{\partial \bar{x}}\left(\bar{k}\,\frac{\partial \overline{T}}{\partial \bar{x}}\right)$ deleted, the governing equations are as follows:

Continuity Equation:

$$\frac{\partial \overline{\rho}\,\overline{u}}{\partial \bar{x}} + \frac{\partial \overline{\rho}\,\overline{v}}{\partial \bar{y}} = 0 \tag{1}$$

x-Momentum Equation:

$$\overline{\rho}\,\overline{u}\,\frac{\partial \overline{u}}{\partial \bar{x}} - \overline{\rho}\,\overline{v}\,\frac{\partial \overline{u}}{\partial \bar{y}} = -\frac{\partial \overline{p}}{\partial \bar{x}} + \frac{\partial}{\partial \bar{y}}\left[\bar{\mu}\left(\frac{\partial \overline{u}}{\partial \bar{y}} - \frac{\partial \overline{v}}{\partial \bar{x}}\right)\right] + \frac{\partial}{\partial \bar{x}}\left[\left(\bar{\mu}_B - \frac{2}{3}\bar{\mu}\right)\frac{\partial \overline{v}}{\partial \bar{y}}\right] \tag{2}$$

y-Momentum Equation:

$$\overline{\rho}\,\overline{u}\,\frac{\partial \overline{v}}{\partial \bar{x}} + \overline{\rho}\,\overline{v}\,\frac{\partial \overline{v}}{\partial \bar{y}} = -\frac{\partial \overline{p}}{\partial \bar{y}} + \frac{\partial}{\partial \bar{y}}\left(\frac{4}{3}\bar{\mu}\,\frac{\partial \overline{v}}{\partial \bar{y}} - \frac{2}{3}\bar{\mu}\,\frac{\partial \overline{u}}{\partial \bar{x}}\right) - \frac{\partial}{\partial \bar{x}}\left(\bar{\mu}\,\frac{\partial \overline{u}}{\partial \bar{y}}\right) + \frac{\partial}{\partial \bar{y}}\left[\bar{\mu}_B\left(\frac{\partial \overline{u}}{\partial \bar{x}} + \frac{\partial \overline{v}}{\partial \bar{y}}\right)\right] \tag{3}$$

Energy Equation:

$$\bar{\rho}\bar{u}\frac{\partial\bar{h}}{\partial\bar{x}} + \bar{\rho}\bar{v}\frac{\partial\bar{h}}{\partial\bar{y}} = \bar{u}\frac{\partial\bar{p}}{\partial\bar{x}} + \bar{v}\frac{\partial\bar{p}}{\partial\bar{y}} + \frac{\partial}{\partial\bar{y}}\left(\bar{k}\frac{\partial\bar{T}}{\partial\bar{y}}\right)$$

$$+ \bar{\mu}\left[\frac{4}{3}\left(\frac{\partial\bar{u}}{\partial\bar{x}}\right)^2 + \frac{4}{3}\left(\frac{\partial\bar{v}}{\partial\bar{y}}\right)^2 + \left(\frac{\partial\bar{v}}{\partial\bar{x}}\right)^2 + \left(\frac{\partial\bar{u}}{\partial\bar{y}}\right)^2 + 2\frac{\partial\bar{v}}{\partial\bar{x}}\frac{\partial\bar{u}}{\partial\bar{y}} - \frac{4}{3}\frac{\partial\bar{u}}{\partial\bar{x}}\frac{\partial\bar{v}}{\partial\bar{y}}\right] \quad (4)$$

$$+ \mu_B\left[\left(\frac{\partial\bar{u}}{\partial\bar{x}}\right)^2 + 2\frac{\partial\bar{u}}{\partial\bar{x}}\frac{\partial\bar{v}}{\partial\bar{y}} + \left(\frac{\partial\bar{v}}{\partial\bar{y}}\right)^2\right]$$

The fluid under consideration is assumed to be a perfect gas with the following constant specific heats:

$$\bar{p} = \bar{\rho}\bar{R}\bar{T} \quad (5)$$

$$d\bar{h} = \bar{c}_p\, d\bar{T} \quad (6)$$

The dynamic viscosity, μ, and the bulk viscosity, μ_B, are both assumed to be functions only of the static temperature, $\bar{T}$. The mathematical model is completed by specifying boundary and initial conditions for the dependent variables. At the wall, standard slip and temperature jump conditions (Ref. 12) applicable to low-density hypersonic flows are employed along with a condition of zero normal velocity at the plate surface.

$$\bar{u}(\bar{x},0) = \frac{2-\sigma}{\sigma}\left(\bar{\ell}\frac{\partial\bar{u}}{\partial\bar{y}}\right)_{y=0} + \frac{3}{4}\left(\frac{\bar{\mu}}{\bar{\rho}\bar{T}}\frac{\partial\bar{T}}{\partial\bar{x}}\right)_{y=0} \quad (7)$$

$$\bar{T}(\bar{x},0) = \frac{2-\alpha}{\alpha}\frac{2\gamma}{\gamma+1}\left(\frac{\bar{\ell}}{Pr}\frac{\partial\bar{T}}{\partial\bar{y}}\right)_{y=0} + \bar{T}_w(x) \quad (8)$$

$$\bar{v}(\bar{x},0) = 0 \quad (9)$$

In the above equations, σ and α are the accommodations coefficients for momentum and energy, respectively, and $\bar{\ell}$ is the molecular mean free

path. The accommodation coefficients are assumed to be unity corresponding to diffusely reflected molecules with perfect thermal accommodation. The thermal creep term of Eq. (7) is frequently neglected in low-density hypersonic flow studies.

Outside the shock layer, the flow variables assume their free-stream values

$$\bar{u} \to \bar{U}_\infty \quad , \quad \bar{v} \to 0 \, , \quad \bar{T} \to \bar{T}_\infty \quad , \quad \bar{\rho} \to \bar{\rho}_\infty \tag{10}$$

For the case of a plate at angle of attack, the velocity components outside the shock layer become

$$\bar{u} \to \bar{U}_\infty \cos\theta \quad \text{and} \quad \bar{v} \to -\bar{U}_\infty \sin\theta$$

where θ is the angle between the plate surface and the free stream as shown in Fig. 2.

The equations are now put in dimensionless form by the introduction of the following dimensionless variables:

$$u = \frac{\bar{u}}{\bar{U}_\infty} \, , \quad v = \frac{\bar{v}}{\bar{U}_\infty} \, , \quad T = \frac{\bar{T}}{\bar{T}_\infty} \, , \quad \rho = \frac{\bar{\rho}}{\rho_\infty}$$

$$x = \frac{\bar{x}}{\bar{L}} \, , \quad y = \frac{\bar{y}}{\bar{L}} \, , \quad \mu = \frac{\bar{\mu}}{\bar{\mu}_\infty} \, , \quad \mu_B = \frac{\bar{\mu}_B}{\bar{\mu}_\infty} \tag{11}$$

The dimensionless equations and boundary conditions that result are as follows:

Continuity Equation:

$$\frac{\partial \rho u}{\partial x} + \frac{\partial \rho v}{\partial y} = 0 \tag{12}$$

x-Momentum Equation:

$$\rho u \frac{\partial u}{\partial x} + \rho v \frac{\partial u}{\partial y} = -\frac{1}{\gamma M_\infty^2}\left(\rho \frac{\partial T}{\partial x} + T \frac{\partial \rho}{\partial x}\right) + \frac{1}{Re}\left[\mu \frac{\partial^2 u}{\partial y^2} + \frac{\mu}{3}\frac{\partial^2 v}{\partial x \partial y} + \frac{d\mu}{dT}\frac{\partial T}{\partial y}\frac{\partial u}{\partial y}\right.$$

$$\left. + \frac{d\mu}{dT}\frac{\partial T}{\partial y}\frac{\partial v}{\partial x} - \frac{2}{3}\frac{d\mu}{dT}\frac{\partial T}{\partial x}\frac{\partial v}{\partial y} + \frac{\partial}{\partial x}\left(\mu_B \frac{\partial v}{\partial y}\right)\right] \tag{13}$$

y-Momentum Equation:

$$\rho u \frac{\partial u}{\partial x} + \rho v \frac{\partial u}{\partial y} = - \frac{1}{\gamma M_\infty^2}\left(\rho \frac{\partial T}{\partial y} + T \frac{\partial \rho}{\partial y}\right) + \frac{1}{Re}\left[\frac{4}{3}\mu \frac{\partial^2 v}{\partial y^2} + \frac{\mu}{3}\frac{\partial^2 u}{\partial x \partial y} + \frac{4}{3}\frac{d\mu}{dT}\frac{\partial T}{\partial y}\frac{\partial v}{\partial y}\right.$$

$$\left. - \frac{2}{3}\frac{d\mu}{dT}\frac{\partial T}{\partial y}\frac{\partial u}{\partial x} + \frac{d\mu}{dT}\frac{\partial T}{\partial x}\frac{\partial u}{\partial y} + \frac{\partial}{\partial y}\left(\mu_B \frac{\partial u}{\partial x}\right) + \frac{\partial}{\partial y}\left(\mu_B \frac{\partial v}{\partial y}\right)\right] \tag{14}$$

Energy Equation:

$$\rho u \frac{\partial T}{\partial x} + \rho v \frac{\partial T}{\partial y} = -(\gamma - 1)\rho T\left(\frac{\partial u}{\partial x} + \frac{\partial v}{\partial y}\right) + \frac{\gamma}{RePr}\left[\mu \frac{\partial^2 T}{\partial y^2} + \frac{d\mu}{dT}\left(\frac{\partial T}{\partial y}\right)^2\right]$$

$$+ \frac{\gamma(\gamma - 1)M_\infty^2}{Re}\mu\left[\frac{4}{3}\left(\frac{\partial u}{\partial x}\right)^2 + \frac{4}{3}\left(\frac{\partial v}{\partial y}\right)^2 + \left(\frac{\partial v}{\partial x}\right)^2 + \left(\frac{\partial u}{\partial y}\right)^2 + 2\frac{\partial v}{\partial x}\frac{\partial u}{\partial y} - \frac{4}{3}\frac{\partial u}{\partial x}\frac{\partial v}{\partial y}\right]$$

$$+ \frac{\gamma(\gamma - 1)M_\infty^2}{Re}\mu_B\left[\left(\frac{\partial u}{\partial x}\right) + 2\frac{\partial u}{\partial x}\frac{\partial v}{\partial y} + \left(\frac{\partial v}{\partial y}\right)^2\right] \tag{15}$$

In these equations, the pressure has been eliminated in terms of density and temperature by using the equation of state.

The dimensionless boundary conditions are

$$u(x,0) = \frac{2 - \sigma}{\sigma}\ell\left(\frac{\partial u}{\partial y}\right)_{y=0} + \frac{3}{4}\frac{1}{Re}\frac{\mu}{\rho T}\left(\frac{\partial T}{\partial x}\right)_{y=0}$$

$$T(x,0) = \frac{2 - a}{a}\frac{2\gamma}{\gamma - 1}\frac{\ell}{Pr}\left(\frac{\partial T}{\partial y}\right)_{y=0} + T_w(x) \tag{16}$$

where

$$\ell = \frac{\bar{\ell}}{\bar{L}} = \frac{\sqrt{\gamma}\, M_\infty}{Re} \sqrt{\frac{\pi}{2}}\, \frac{\mu}{\rho\sqrt{T}} \tag{17}$$

Outside the shock layer the dependent variables u, T, and ρ all go to unity and v vanishes for zero angle of attack. If the plate is inclined to the free stream at angle θ, then outside the shock layer

$$\rho \to 1 \quad , \quad T \to 1$$
$$u \to \cos\theta \quad , \quad v \to -\sin\theta$$

It should be noted that the explicit Reynolds number dependence can be removed from the equations by defining new dimensionless independent variables

$$x^* = xRe$$
$$y^* = yRe$$

The equations and boundary conditions in x* and y* variables are the same as those in Eqs. (12) through (17) with Re set equal to one. Thus the effect of varying Reynolds number on the solution is simply to change the length scale.

2.2 TRANSFORMATION OF EQUATIONS

In order to approximate the governing partial differential equations accurately with finite-difference equations, it is necessary that the grid point spacing be very small in the compressive shocklike region where abrupt changes occur. It is desirable, therefore, to transform to a new set of independent variables which will expand the compressive region and make the equations more amenable to a finite-difference solution. Since the density is at a maximum in the shocklike region, the Howarth transformation

$$\xi = x \qquad \eta = \int_0^y \rho\, dy \tag{18}$$

produces the desired deformation. Under this transformation the governing equations take the following forms:

Continuity Equation:

$$\frac{\partial \rho u}{\partial \xi} + \frac{\partial \eta}{\partial x}\frac{\partial \rho u}{\partial \eta} + \rho \frac{\partial \rho v}{\partial \eta} = 0 \tag{19}$$

x-Momentum Equation:

$$\begin{aligned}\rho u \frac{\partial u}{\partial x} + \rho^2 v \frac{\partial u}{\partial \eta} = &-\frac{1}{\gamma M_\infty^2}\left(\rho \frac{\partial T}{\partial x} + T\frac{\partial \rho}{\partial x}\right) + \frac{1}{Re}\left[\mu\left(\rho^2\frac{\partial^2 u}{\partial \eta^2} + \rho\frac{\partial \rho}{\partial \eta}\frac{\partial u}{\partial \eta}\right)\right.\\ &+ \mu\left(\frac{1}{3} + \frac{\mu_B}{\mu}\right)\frac{\partial^2 v}{\partial x \partial y} + \rho^2\frac{d\mu}{dT}\frac{\partial T}{\partial \eta}\frac{\partial u}{\partial \eta} + \rho\frac{d\mu}{dT}\frac{\partial T}{\partial \eta}\frac{\partial v}{\partial x}\\ &\left.+ \left(\frac{\mu_B}{\mu} - \frac{2}{3}\right)\rho\frac{d\mu}{dT}\frac{\partial v}{\partial \eta}\frac{\partial T}{\partial x}\right]\end{aligned} \tag{20}$$

y-Momentum Equation:

$$\begin{aligned}\rho u \frac{\partial v}{\partial x} + \rho^2 v \frac{\partial v}{\partial \eta} = &-\frac{1}{\gamma M_\infty^2}\left(\rho^2\frac{\partial T}{\partial \eta} + T\rho\frac{\partial T}{\partial \eta}\right) + \frac{1}{Re}\left[\mu\left(\frac{4}{3} + \frac{\mu_B}{\mu}\right)\left(\rho^2\frac{\partial^2 v}{\partial \eta^2} + \rho\frac{\partial \rho}{\partial \eta}\frac{\partial v}{\partial \eta}\right)\right.\\ &+ \mu\left(\frac{1}{3} - \frac{\mu_B}{\mu}\right)\frac{\partial^2 u}{\partial x \partial y} + \left(\frac{4}{3} + \frac{\mu_B}{\mu}\right)\rho^2\frac{d\mu}{dT}\frac{\partial T}{\partial \eta}\frac{\partial v}{\partial \eta}\\ &\left.+ \left(\frac{\mu_B}{\mu} - \frac{2}{3}\right)\rho\frac{d\mu}{dT}\frac{\partial T}{\partial \eta}\frac{\partial u}{\partial x} + \rho\frac{d\mu}{dT}\frac{\partial T}{\partial x}\frac{\partial u}{\partial \eta}\right]\end{aligned} \tag{21}$$

Energy Equation:

$$\begin{aligned}\rho u \frac{\partial T}{\partial x} + \rho^2 v \frac{\partial T}{\partial \eta} = &-(\gamma - 1)\rho T\left(\frac{\partial u}{\partial x} + \rho\frac{\partial v}{\partial \eta}\right) + \frac{\gamma}{RePr}\left[\rho^2\mu\frac{\partial^2 T}{\partial \eta^2} + \rho\mu\frac{\partial \rho}{\partial \eta}\frac{\partial T}{\partial \eta} + \rho^2\frac{d\mu}{dT}\left(\frac{\partial T}{\partial \eta}\right)^2\right]\\ &+ \frac{\gamma(\gamma-1)M_\infty^2}{Re}\mu\left\{\left(\frac{4}{3} + \frac{\mu_B}{\mu}\right)\left[\left(\frac{\partial u}{\partial x}\right)^2 + \rho^2\left(\frac{\partial v}{\partial \eta}\right)^2\right]\right.\\ &\left.+ \left(\frac{\partial v}{\partial x}\right)^2 + \rho^2\left(\frac{\partial u}{\partial \eta}\right)^2 - 2\rho\frac{\partial v}{\partial x}\frac{\partial u}{\partial \eta} + \left(2\frac{\mu_B}{\mu} - \frac{4}{3}\right)\rho\frac{\partial u}{\partial x}\frac{\partial v}{\partial \eta}\right\}\end{aligned} \tag{22}$$

where

$$\frac{\partial}{\partial x} = \frac{\partial}{\partial \xi} + \frac{\partial \eta}{\partial x}\frac{\partial}{\partial \eta} \tag{23}$$

$$\frac{\partial^2}{\partial x \partial y} = \rho \frac{\partial^2}{\partial \xi \partial \eta} + \rho \frac{\partial \eta}{\partial x}\frac{\partial^2}{\partial \eta^2} + \frac{\partial^2 \eta}{\partial x \partial y}\frac{\partial}{\partial \eta} \tag{24}$$

Equations (19) through (22) are the equations that were programmed for solution. It is evident that the Howarth transformation substantially complicates the equations algebraically. In particular, the derivative $\frac{\partial \eta}{\partial x}$ does not cancel out as in the boundary-layer case; hence this term must be evaluated in the course of the solution.

2.3 CONICAL FLOW

The governing equations for axially symmetric flow about a sharp conical body have also been formulated for solution on a digital computer. The geometry and nomenclature for flow about a sharp cone are shown in Fig. 3.

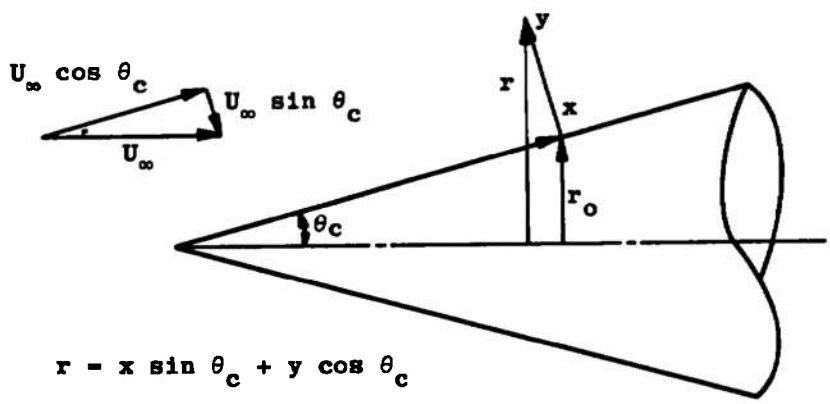

Fig. 3 Geometry and Coordinate System for Axisymmetric Flow

The continuity equation for axially symmetric flow in the notation shown above is

$$\frac{\partial}{\partial x}(\rho u r) + \frac{\partial}{\partial y}(\rho v r) = 0 \tag{25}$$

After transforming to (ξ, η) variables the continuity equation is

$$\frac{\partial \rho u}{\partial \xi} + \frac{\partial \eta}{\partial x}\frac{\partial \rho u}{\partial \eta} + \rho\frac{\partial \rho v}{\partial \eta} + \rho\left(\frac{\sin\theta_c}{r}u + \frac{\cos\theta_c}{r}v\right) = 0 \tag{26}$$

This equation differs from the continuity equation for two-dimensional flow, Eq. (19), only by the final term. In like manner the x-momentum equation, (20), the y-momentum equation, (21), and the energy equation, (22), for two-dimensional flow can be adapted to the flow about a cone by the addition of the following terms to the right-hand side of those equations: To the x-momentum equation, Eq. (20), add

$$\begin{aligned}\frac{1}{rRe}\Bigg\{&\left[2\mu + \left(\frac{\mu_B}{\mu} - \frac{2}{3}\right)\mu\sin\theta_c\right]\frac{\partial u}{\partial x} + \rho\mu\cos\theta_c\frac{\partial u}{\partial \eta} + \left[\left(\frac{\mu_B}{\mu} - \frac{2}{3}\right)\sin\theta_c\frac{d\mu}{dT}\frac{\partial T}{\partial x}\right.\\ &\left. - \left(\frac{\mu_B}{\mu} - \frac{2}{3}\right)\mu\frac{\sin^2\theta_c}{r} - \frac{2\mu}{r}\sin\theta_c\right]u + \left[\left(\frac{\mu_B}{\mu} - \frac{2}{3}\right)\cos\theta_c\frac{d\mu}{dT}\frac{\partial T}{\partial x}\right.\\ &\left. - \left(\frac{\mu_B}{\mu} - \frac{2}{3}\right)\mu\frac{\sin\theta_c\cos\theta_c}{r} - \frac{2\mu\cos\theta_c}{r}\right]v + \left(\frac{\mu_B}{\mu} + \frac{1}{3}\right)\cos\theta_c\mu\frac{\partial v}{\partial x}\Bigg\}\end{aligned} \tag{27}$$

To the y-momentum equation, Eq. (21), add

$$\begin{aligned}\frac{1}{rRe}\Bigg\{&\left(\frac{\mu_B}{\mu} + \frac{1}{3}\right)\sin\theta_c\rho\mu\frac{\partial u}{\partial \eta} + \left(\frac{\mu_B}{\mu} + \frac{4}{3}\right)\cos\theta_c\rho\mu\frac{\partial v}{\partial \eta} + \sin\theta_c\mu\frac{\partial v}{\partial x}\\ &+ \left[\left(\frac{\mu_B}{\mu} - \frac{2}{3}\right)\sin\theta_c\rho\frac{d\mu}{dT}\frac{\partial T}{\partial \eta} - \left(\frac{\mu_B}{\mu} - \frac{4}{3}\right)\frac{\sin\theta_c\cos\theta_c}{r}\mu\right]v\\ &+ \left[\left(\frac{\mu_B}{\mu} - \frac{2}{3}\right)\cos\theta_c\rho\frac{d\mu}{dT}\frac{\partial T}{\partial \eta} - \left(\frac{\mu_B}{\mu} - \frac{4}{3}\right)\frac{\cos^2\theta_c}{r}\mu\right]v\Bigg\}\end{aligned} \tag{28}$$

To the Energy equation, Eq. (22), add

$$\begin{aligned}&\frac{\gamma}{RePr}\mu\left(\frac{\sin\theta_c}{r}\frac{\partial T}{\partial x} + \frac{\cos\theta_c}{r}\rho\frac{\partial T}{\partial \eta}\right) - (\gamma - 1)\rho T\left(\frac{\sin\theta_c}{r}\mu + \frac{\cos\theta_c}{r}v\right)\\ &+ \frac{\gamma(\gamma-1)M_\infty^2}{Re}\mu\left[\left(2\frac{\mu_B}{\mu} - \frac{4}{3}\right)\left(\frac{\sin\theta_c}{r}u + \frac{\cos\theta_c}{r}v\right)\left(\frac{\partial u}{\partial x} + \rho\frac{\partial v}{\partial \eta}\right)\right.\\ &\left. + \left(\frac{\mu_B}{\mu} + \frac{4}{3}\right)\left(\frac{\sin\theta_c}{r}u + \frac{\cos\theta_c}{r}v\right)^2\right]\end{aligned} \tag{29}$$

In the above expressions, $\frac{\partial}{\partial x}$ represents the differential operation, Eq. (23).

Equations (19) through (22) and corresponding equations (including the conical flow terms) were programmed for numerical solution on a digital computer. The solution technique used is discussed in detail in the following section.

SECTION III
SOLUTION PROCEDURE

3.1 FINITE-DIFFERENCE EQUATIONS

Following Blottner (Ref. 13) and Davis (Ref. 14), one can write Eqs. (20) through (22), the momentum equations and the energy equation, in standard form, which is convenient for the numerical solution technique.

$$\frac{\partial^2 w}{\partial \eta^2} + a_1 \frac{\partial w}{\partial \eta} + a_2 w + a_3 + a_4 \frac{\partial w}{\partial \xi} = 0 \tag{30}$$

The coefficients α_1, α_2, α_3, and α_4 are, in general, functions of the dependent variables of the problem and are therefore unknown. These coefficients must be determined by an iterative procedure and will, for the moment, be assumed to be known functions of the independent variables, η. Put in this form, the x-momentum equation, Eq. (20), becomes

$$\frac{\partial^2 u}{\partial \eta^2} + a_{u1} \frac{\partial u}{\partial \eta} + a_{u2} u + a_{u3} + a_{u4} \frac{\partial u}{\partial \xi} = 0 \tag{31}$$

where

$$a_{u1} = \frac{1}{\rho}\frac{\partial \rho}{\partial \eta} + \frac{1}{\mu}\frac{d\mu}{dT}\frac{\partial T}{\partial \eta} - \frac{Re\, u}{\rho\mu}\frac{\partial \eta}{\partial x} - \frac{Re\, v}{\mu}$$

$$a_{u2} = 0$$

$$a_{u3} = -\frac{Re}{\rho^2 \mu \gamma M_\infty^2}\frac{\partial \rho T}{\partial x} + \frac{1}{\rho^2}\left(\frac{1}{3} + \frac{\mu_B}{\mu}\right)\frac{\partial^2 v}{\partial x \partial y} + \frac{1}{\rho\mu}\frac{d\mu}{dT}\frac{\partial T}{\partial \eta}\frac{\partial v}{\partial x} + \frac{1}{\rho\mu}\left(\frac{\mu_B}{\mu} - \frac{2}{3}\right)\frac{d\mu}{dT}\frac{\partial v}{\partial \eta}\frac{\partial T}{\partial x}$$

$$a_{u4} = -\frac{u\, Re}{\rho\mu} \tag{32}$$

The y-momentum equation becomes

$$\frac{\partial^2 v}{\partial \eta^2} + a_{v1}\frac{\partial v}{\partial \eta} + a_{v2}v - a_{v3} + a_{v4}\frac{\partial v}{\partial \xi} = 0 \tag{33}$$

where

$$\begin{aligned}
a_{v1} &= \frac{1}{\rho}\frac{\partial \rho}{\partial \eta} + \frac{1}{\mu}\frac{d\mu}{dT}\frac{\partial T}{\partial \eta} - \frac{3\,Re}{\mu\beta_\mu}\left(v + \frac{u}{\rho}\frac{\partial \eta}{\partial x}\right)\\
a_{v2} &= 0\\
a_{v3} &= -\frac{3\,Re}{\rho^2\mu\gamma M_\infty^2\beta_\mu}\left(\rho^2\frac{\partial T}{\partial \eta} + \rho T\frac{\partial \rho}{\partial \eta}\right) + \frac{1}{\rho^2}\frac{1 + 3(\mu_B/\mu)}{\beta_\mu}\frac{\partial^2 u}{\partial x \partial y}\\
&\quad + \frac{1}{\rho\mu}\frac{3(\mu_B/\mu) - 2}{\beta_\mu}\frac{d\mu}{dT}\frac{dT}{d\eta}\frac{\partial u}{\partial x} - \frac{3}{\beta_\mu}\frac{1}{\rho\mu}\frac{d\mu}{dT}\frac{\partial T}{\partial x}\frac{\partial u}{\partial \eta}\\
a_{v4} &= -\frac{u}{\rho\mu}\frac{3\,Re}{\beta_\mu}\\
\beta_\mu &= 4 + 3(\mu_B/\mu)
\end{aligned} \tag{34}$$

The energy equation becomes

$$\frac{\partial^2 T}{\partial \eta^2} + a_{T1}\frac{\partial T}{\partial \eta} + a_{T2}T + a_{T3} + a_{T4}\frac{\partial T}{\partial \xi} = 0 \tag{35}$$

where

$$\begin{aligned}
a_{T1} &= \frac{1}{\rho}\frac{\partial \rho}{\partial \eta} + \frac{1}{\mu}\frac{d\mu}{dT}\frac{\partial T}{\partial \eta} - \frac{v\,Re\,Pr}{\gamma\mu} - \frac{u\,Re\,Pr}{\rho\mu\gamma}\frac{\partial \eta}{\partial x}\\
a_{T2} &= -\frac{(\gamma - 1)Re\,Pr}{\rho\mu\gamma}\left(\frac{\partial u}{\partial x} + \rho\frac{\partial v}{\partial \eta}\right)\\
a_{T3} &= \frac{(\gamma - 1)Pr\,M_\infty^2}{\rho^2}\left[\frac{\beta_\mu}{3}\left(\frac{\partial u}{\partial x}\right)^2 - \frac{\beta_\mu}{3}\rho^2\left(\frac{\partial v}{\partial \eta}\right)^2 + \left(\frac{\partial v}{\partial x}\right)^2 + \rho^2\left(\frac{\partial u}{\partial \eta}\right)^2 + 2\rho\frac{\partial v}{\partial x}\frac{\partial u}{\partial \eta}\right.\\
&\quad \left. + \frac{6(\mu_B/\mu) - 4}{3}\rho\frac{\partial u}{\partial x}\frac{\partial v}{\partial \eta}\right]\\
a_{T4} &= -\frac{Re\,Pr}{\rho\mu\gamma}u
\end{aligned} \tag{36}$$

Equation (30) can be approximated by a finite-difference equation at the general point of the flow field m + 1, n, using equally spaced central differences for the η derivatives and a two-point backward difference for the ξ derivative. This is illustrated schematically in Fig. 4.

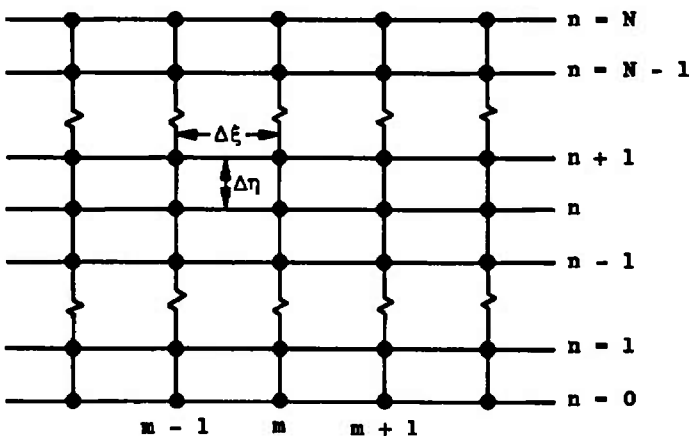

Fig. 4 Finite-Difference Grid

Thus, let

$$\left(\frac{\partial w}{\partial \xi}\right)_{m+1,n} = \frac{w_{m+1,n} - w_{m,n}}{\Delta \xi} + 0(\Delta \xi)$$

$$\left(\frac{\partial w}{\partial \eta}\right)_{m+1,n} = \frac{w_{m+1,n+1} - w_{m+1,n-1}}{2\Delta \eta} - 0(\Delta \eta^2) \qquad (37)$$

$$\left(\frac{\partial^2 w}{\partial \eta^2}\right)_{m+1,n} = \frac{w_{m+1,n+1} - 2w_{m+1,n} + w_{m+1,n-1}}{\Delta \eta^2} - 0(\Delta \eta^2)$$

Substituting into Eq. (30), a finite-difference equation is obtained, as follows:

$$\frac{w_{m+1,n+1} - 2w_{m+1,n} + w_{m+1,n-1}}{\Delta \eta^2} + a_1^{m+1,n} \frac{w_{m+1,n+1} - w_{m+1,n-1}}{2\Delta \eta}$$

$$+ a_2^{m+1,n} w_{m+1,n} + a_3^{m+1,n} + a_4^{m+1,n} \frac{w_{m+1,n} - w_{m,n}}{\Delta \xi} = 0$$

The coefficients $\alpha_i^{m+1,n}$ are the values of α at m + 1, n and are assumed to be known. In addition, the values $w_{m,n}$ at the proceeding station are assumed known. This equation for the three unknowns $w_{m+1,n+1}$, $w_{m+1,n}$, and $w_{m+1,n-1}$ can be written in the form

$$A_n w_{n-1} + B_n w_n + C_n w_{n+1} = D_n \tag{38}$$

where

$$\begin{aligned} A_n &= \left(\frac{\Delta\xi}{\Delta\eta^2} - \frac{a_1^n \Delta\xi}{2\Delta\eta}\right) \\ B_n &= \left(-\frac{2\Delta\xi}{\Delta\eta^2} + a_2^n \Delta\xi + a_4^n\right) \qquad 2 \le n \le N-1 \\ C_n &= \left(\frac{\Delta\xi}{\Delta\eta^2} + \frac{a_1^n \Delta\xi}{2\Delta\eta}\right) \\ D_n &= -a_3^n \Delta\xi + a_4^n w_{m,n} \end{aligned} \tag{39}$$

One such finite-difference equation is applicable at each interior point n at ξ station m + 1. Information about the value of w at n = 1 and at n = N is supplied by the boundary conditions. At y = 0 the boundary conditions for u, v, or T can each be expressed in the general form

$$w(\xi,o) = k_1 \left(\frac{\partial w}{\partial \eta}\right)_{n=o} + k_2 \tag{40}$$

Using the formula

$$\left(\frac{\partial w}{\partial \eta}\right)_{\eta=o} = \frac{4w_2 - 3w_1 - w_3}{2\Delta\eta} + O(\Delta\eta^2)$$

this can be written in finite-difference form as

$$A_1 w_1 + B_1 w_2 + C_1 w_3 = D_1 \tag{41}$$

where

$$\begin{aligned} A_1 &= 1 + \frac{3k_1}{2\Delta\eta} & B_1 &= -\frac{2k_1}{\Delta\eta} \\ C_1 &= \frac{k_1}{\Delta\eta} & D_1 &= k_2 \end{aligned} \tag{42}$$

The outer boundary condition for all three variables, u, v, and T, is of the form

$$w_N = D_N$$

where D_N is a known constant. Thus the w profile at ξ station m + 1 is given by the system of linear algebraic equations

$$\begin{bmatrix} A_1 & B_1 & C_1 & 0 & \cdot & \cdot & \cdot & 0 \\ A_2 & B_2 & C_2 & 0 & \cdot & \cdot & \cdot & 0 \\ 0 & A_3 & B_3 & C_3 & 0 & \cdot & \cdot & 0 \\ 0 & \cdot & A_4 & B_4 & C_4 & 0 & \cdot & 0 \\ 0 & \cdot & \cdot & \cdot & \cdot & \cdot & \cdot & 0 \\ 0 & \cdot & \cdot & \cdot & \cdot & \cdot & \cdot & 0 \\ 0 & \cdot & \cdot & \cdot & \cdot & A_{N-1} & B_{N-1} & C_{N-1} \\ 0 & \cdot & \cdot & \cdot & \cdot & 0 & 0 & 1 \end{bmatrix} \times \begin{bmatrix} w_1 \\ w_2 \\ w_3 \\ \\ \\ \\ w_{N-1} \\ w_N \end{bmatrix} = \begin{bmatrix} D_1 \\ D_2 \\ D_3 \\ \\ \\ \\ D_{N-1} \\ D_N \end{bmatrix} \tag{43}$$

Because of the special form of the coefficient matrix there is a very efficient algorithm given by Richtmyer and Morton (Ref. 15) that can be used to solve these equations. The recursion formulas for w are as follows:

$$w_n = E_n w_{n-1} - F_n \qquad 2 \le n \le N-1 \tag{44}$$

$$w_1 = E_1 w_2 + F_1 w_3 + G_1 \tag{45}$$

where

$$\begin{aligned} E_2 &= -\frac{C_2 + A_2 F_1}{B_2 + A_2 E_1} \\ F_2 &= \frac{D_2 - G_1 A_2}{B_2 + A_2 E_1} \\ E_n &= \frac{-C_n}{B_n + A_n E_{n-1}} \qquad n = 3, 4, \cdots N-1 \\ F_n &= \frac{D_n - A_n F_{n-1}}{B_n + A_n E_{n-1}} \end{aligned} \tag{46}$$

The equations for w_n can be solved using a double-sweep technique; marching out from n = 1 calculating the coefficients E_n and F_n, and then marching back from n = N computing w_n.

With this procedure, the x- and y-momentum equations and the energy equation can be solved to obtain u, v, and T profiles. These values can then be used in computing improved coefficients α_1, α_2, α_3, and α_4. The density, however, must be computed from the continuity equation using a different procedure. The method described below is one of many possible methods that could be employed. Expanding the continuity equation and solving for $\frac{\partial \rho}{\partial \xi}$ gives

$$\frac{\partial \rho}{\partial \xi} = -\frac{\rho}{u}\frac{\partial u}{\partial \xi} - \frac{\rho}{u}\frac{\partial \eta}{\partial y}\frac{\partial u}{\partial \eta} - \frac{\partial \eta}{\partial y}\frac{\partial \rho}{\partial \eta} - \frac{\rho^2}{u}\frac{\partial v}{\partial \eta} - \frac{\rho v}{u}\frac{\partial \rho}{\partial \eta} \tag{47}$$

Assuming that trial u, v, and ρ profiles at m + 1 are known, the right side of this equation can be evaluated at each point n at station m + 1. Then an improved value of ρ is obtained from the equation

$$\rho_{m+1,n} = \rho_{m,n} + \frac{\Delta \xi}{2}\left[\left(\frac{\partial \rho}{\partial \xi}\right)_{m,n} + \left(\frac{\partial \rho}{\partial \xi}\right)_{m+1,n}\right] \tag{48}$$

Note that the calculation breaks down if there is no slip between the wall and the fluid. Slip boundary conditions were used in all calculations. From the density profile it is possible to compute values of $\frac{\partial \eta}{\partial x}$ for use in the next iteration and at the same time perform the inverse transformation

$$\begin{aligned} y &= \int_0^{\eta} \frac{1}{\rho}\, d\eta \quad , \quad x = \xi \\ \frac{\partial \eta}{\partial y} &= -\rho\left(\frac{\partial y}{\partial \xi}\right)_{\eta} \end{aligned} \tag{49}$$

The whole calculation procedure can be repeated to obtain improved values of the flow variables u, v, T, and ρ. This iteration is continued until the values for successive calculations are within prescribed limits. All other pertinent flow quantities can be obtained from these profiles.

3.2 COMPUTER PROGRAM

A flow chart showing the steps of the calculation procedure and the basic subroutines of the computer program is shown in Fig. 5. (Only the essential features of the computer program are shown in the diagram). In this flow chart the symbol W(J) is used to represent all four flow variables, u, v, T, and ρ. The symbol WO(J) refers to values at the previous station, and WL(J) refers to values obtained from the last iteration. The function of the major subroutines called in the program is described below:

SUBROUTINE READIN - Reads the parameters for the calculations from data cards and defines the initial profiles for u, v, T, and ρ.

SUBROUTINE WALL - Calculates coefficients E_1, F_1, and G_1 in Eq. (45) from boundary conditions.

SUBROUTINE COEF - Calculates α coefficients based on values from the last iteration. Calculates the finite-difference coefficients A_n, B_n, C_n, and D_n.

SUBROUTINE SOLVE - Solves the finite-difference equations, Eqs. (43), by recursion formulas, Eqs. (44) and (45).

SUBROUTINE RHO - Calculates density profile using Eq. (48). Iterates to convergence.

SUBROUTINE ETA - Calculates y, the distance from the wall, and $\frac{\partial \eta}{\partial x}$.

SUBROUTINE RITE - Computes the pertinent parameters such as heat-transfer rate and skin friction and prints results.

The calculations were generally begun using uniform initial profiles for the gas dynamic variables described by 25 points across the shock layer with a $\Delta\eta$ of 0.02. Additional points were added as the calculation proceeded downstream and the shock-layer thickness increased. The maximum number of points that could be used was 501, and this was usually sufficient to describe the shock layer in the region of interest without increasing $\Delta\eta$. The small $\Delta\eta$ was required to obtain sufficient resolution in the shock wave region and resulted in long computation times. The time required to run a typical case was between one and two hours on the CDC 1604-B computer. The longitudinal step size $\Delta\xi$ was usually set equal to $\Delta\eta$ initially, but was multiplied by a growth factor of less than one percent after each step.

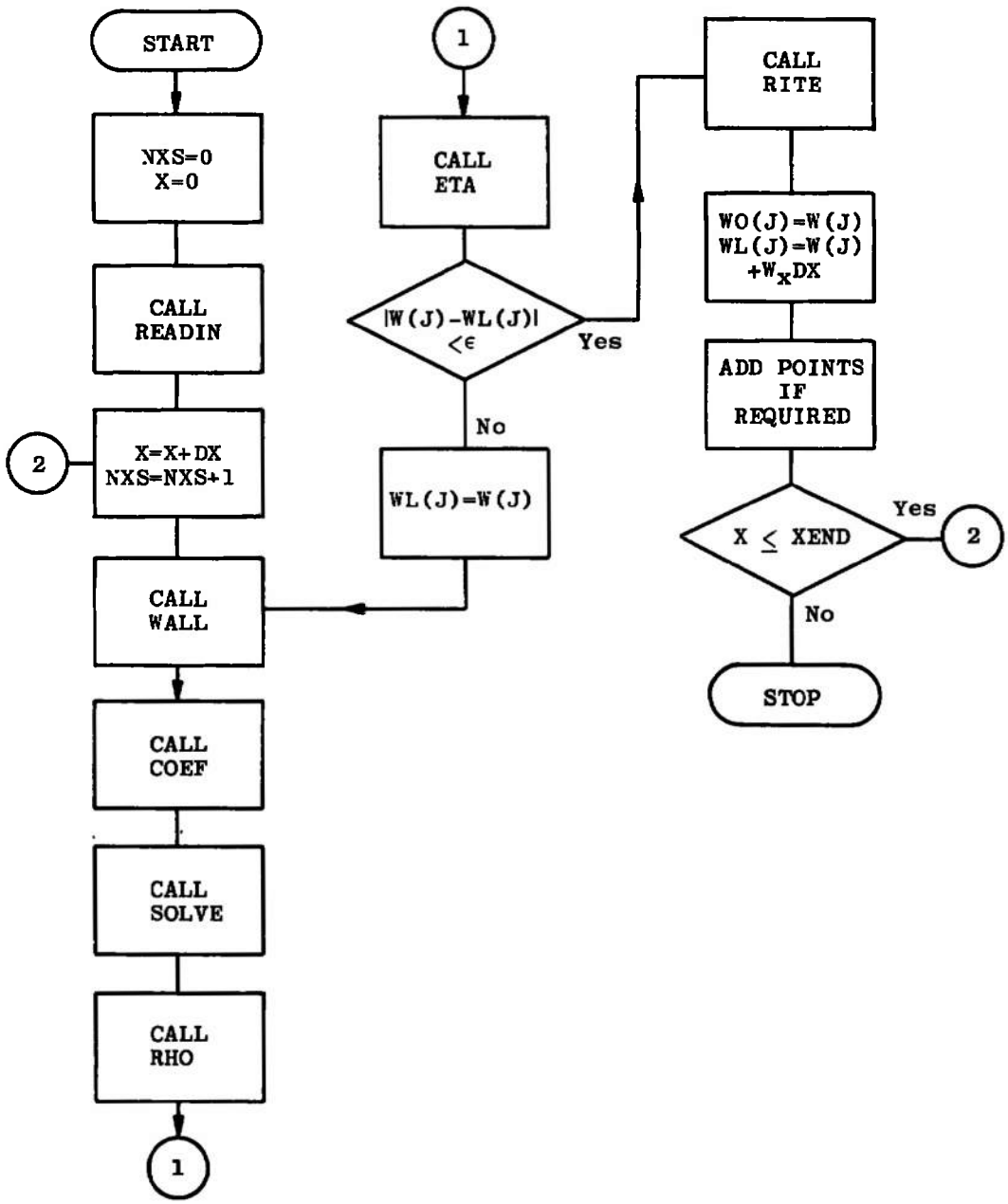

Fig. 5 Flow Chart for Computer Program

An iteration procedure was required to determine the coefficients of the linearized governing equations. The convergence of this iteration was determined by testing the change in the solution between successive iterations. A convergence criterion of 0.1 percent was found to yield acceptable accuracy without an excessive number of iterations.

Failure of the calculation procedure occurred for several cases at large values of x. The failure seemed to be associated with a decrease in the slip velocity at the wall and was preceded by oscillations in $\partial v/\partial \eta$ near $\eta = 0$. These oscillations increased in magnitude and finally destroyed the calculation. As noted earlier, when the slip velocity becomes small, the wall density as computed by Eq. (47) becomes very questionable. It is likely that this is at least partly responsible for the calculation difficulties at large values of x. When calculation failure occurred, the hypersonic interaction parameter, $\overline{\chi}$, was always less than 0.25, indicating that the flow was well beyond the merged regime.

SECTION IV
CALCULATION RESULTS

4.1 TYPICAL PROFILES

Some typical results of the calculation procedure described in the previous section are presented in Figs. 6 through 13. The free-stream flow conditions used for this calculation correspond to flat-plate data collected by Becker and Boylan (Ref. 16) in the von Kármán Facility (VKF) Low Density Hypersonic Wind Tunnel (L) and are tabulated below:

$$M_\infty = 9.19$$

$$p_\infty = 55\mu\text{Hg}$$

$$T_\infty = 96°\text{K}$$

$$\text{Re}/\overline{L} = 1660/\text{in.}$$

$$\gamma = 1.4$$

$$T_w = 300°\text{K}$$

$$P_r = 0.71$$

The values for viscosity used in the calculation were obtained from the Sutherland formula with the constants appropriate for nitrogen.

Figures 6 through 9 show the flow variable profiles and illustrate quite clearly the transition from a merged flow region where the shock is buried in the viscous region to the strong interaction regime where a rather well-defined shock exists. The velocity profiles in Fig. 6, for example, exhibit a relatively large slip velocity near the leading edge but otherwise appear well behaved. Further downstream a point of inflection develops that is associated with the formation of the compressive shocklike region. This point in the velocity profile becomes more pronounced as the flow proceeds downstream. The later profiles show an inviscid region beginning to form between the shock and the

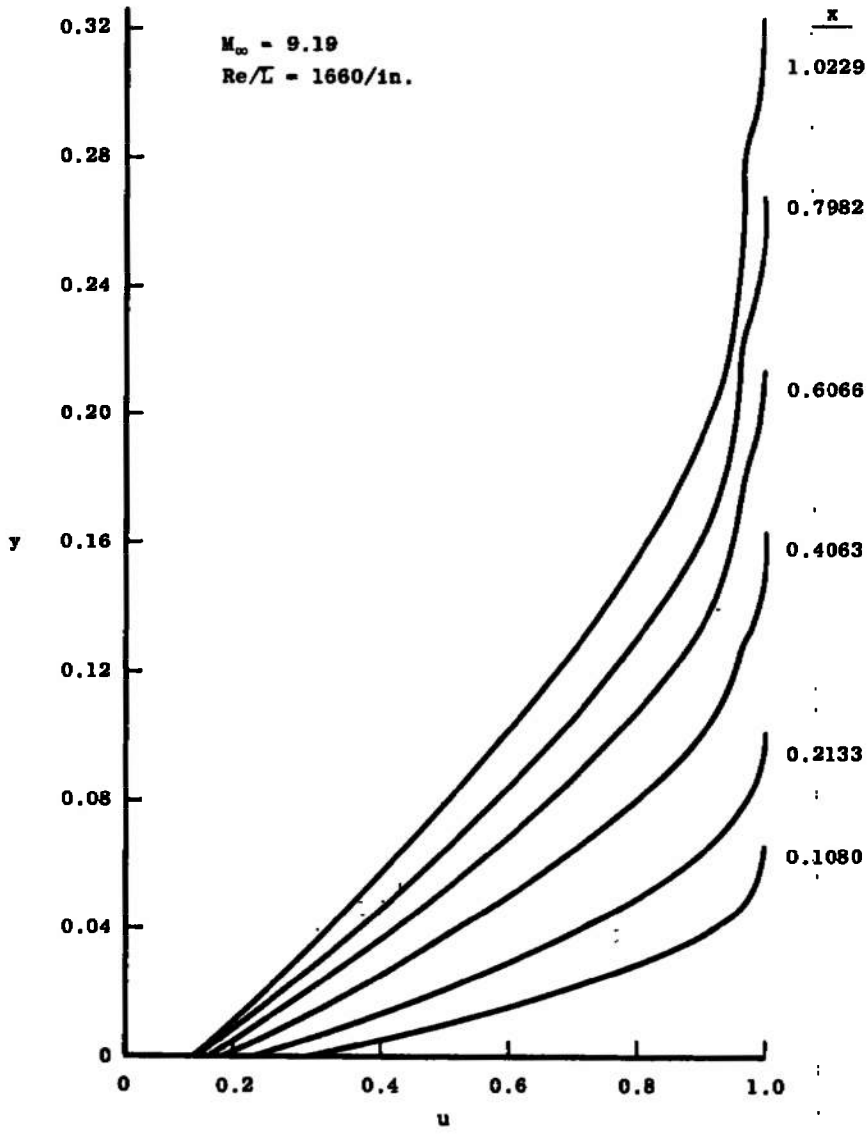

Fig. 6 Typical Velocity Profiles

viscous boundary layer. The other flow variables show a corresponding evolution from the merged region to the strong interaction region. The pressure profiles are particularly revealing with regard to the development of the shock. Near the leading edge there is a pronounced pressure variation in the y-direction throughout the viscous shock layer. Farther downstream the pressure variation is largely confined to the outer part of the shock layer, and there is a substantial portion of the flow field where the boundary-layer approximation $\partial p/\partial y = 0$ is valid.

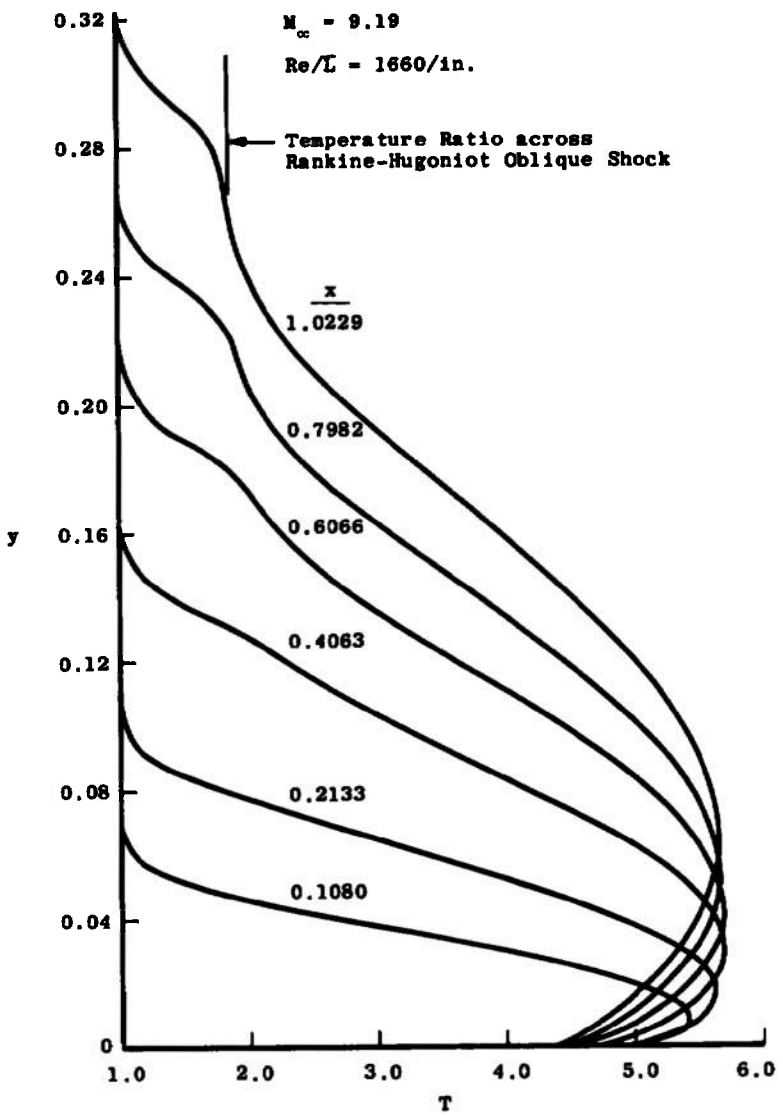

Fig. 7 Typical Temperature Profiles

The center of the shock structure can be fairly well defined by the peak in the density profiles (see Fig. 9). The locus of these density peaks is plotted in Fig. 11 to show the location of the shock wave relative to the plate. The shock is slightly curved near the leading edge, becoming straight and oriented at 13.4 deg to the plate surface further downstream. The temperature and pressure behind a Rankine-Hugoniot oblique shock oriented at the angle with M_∞ = 9.19 are shown for reference in Figs. 7 and 8.

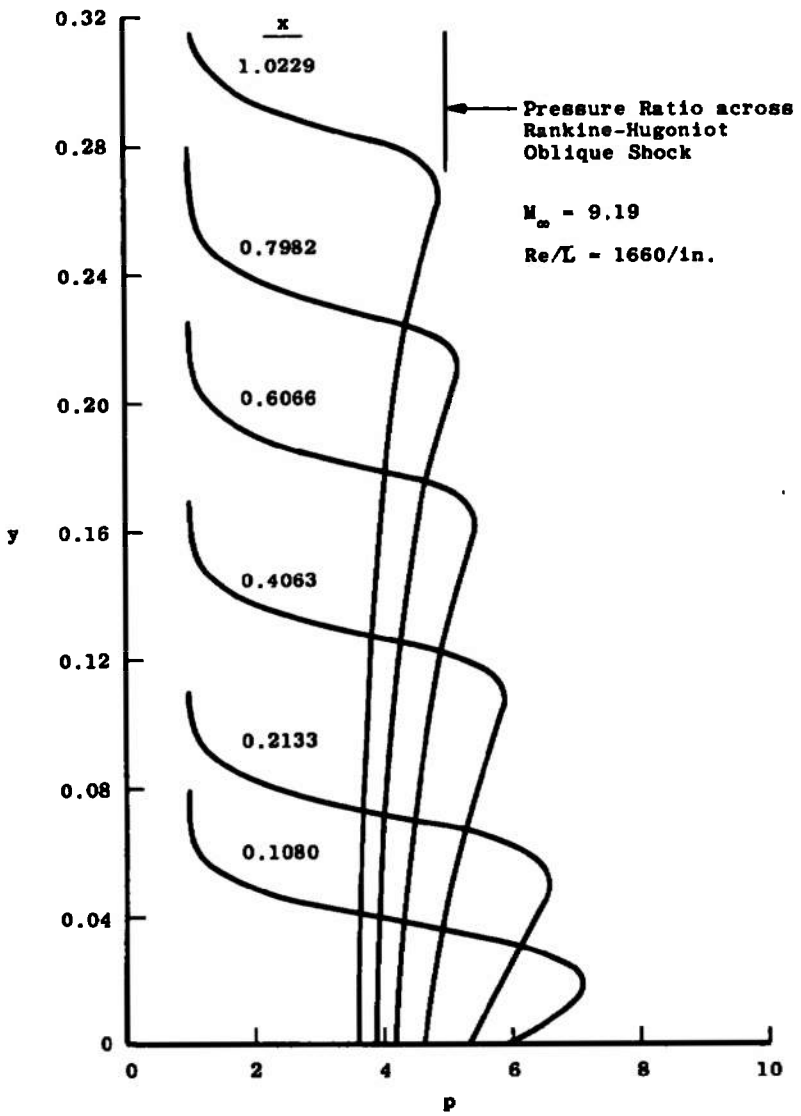

Fig. 8 Typical Pressure Profiles

The variations of gas velocity, temperature, and pressure at the plate surface are shown in Fig. 12. The solutions were started with uniform profiles at x = 0 (i.e., perfect slip); as expected, the slip velocity decreases as distance along the plate increases. The pressure increases rapidly from the initial free-stream value to a maximum of about 6 p_∞ and then slowly decreases. The surface gas temperature exhibits a similar behavior. Figure 13 shows that the skin friction coefficient and the Stanton number display the expected trends.

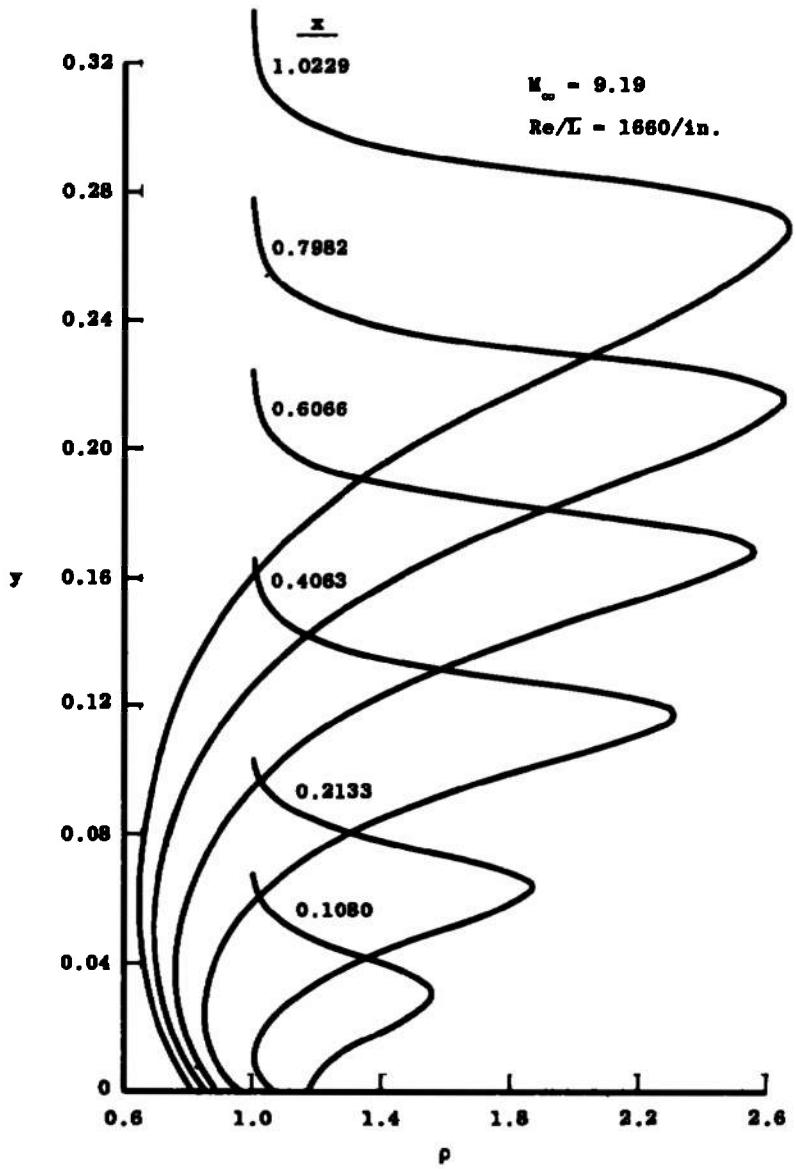

Fig. 9 Typical Density Profiles

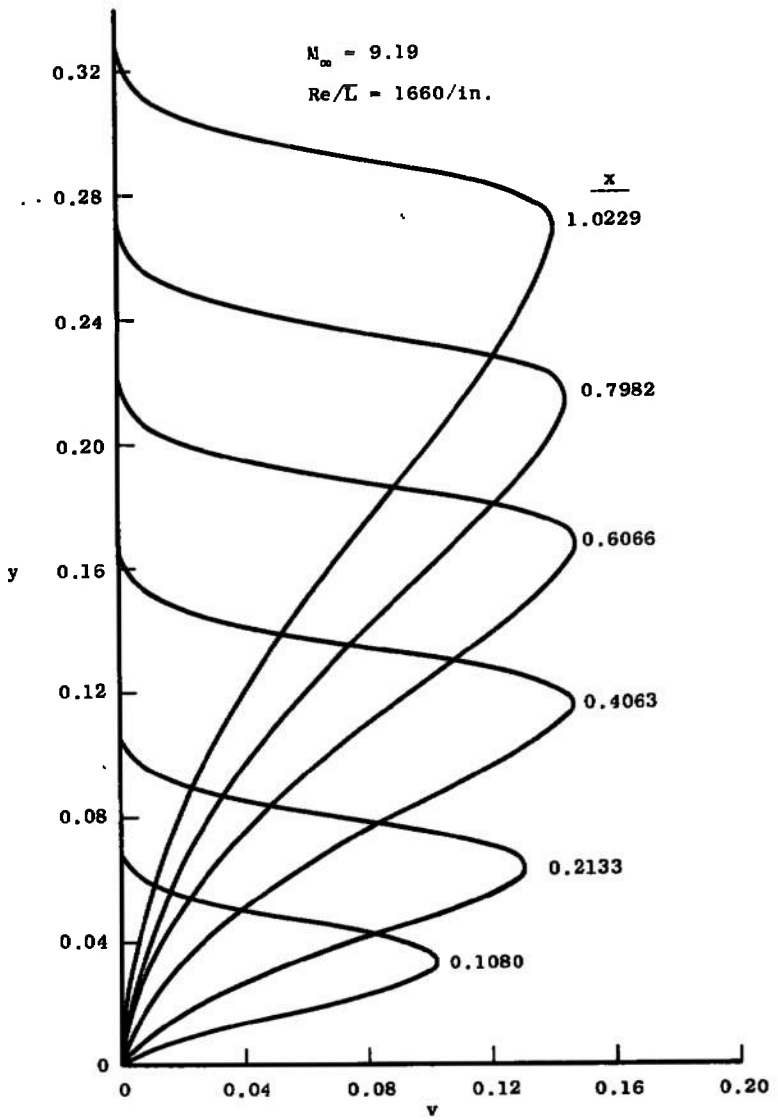

Fig. 10 Typical Transverse Velocity Profiles

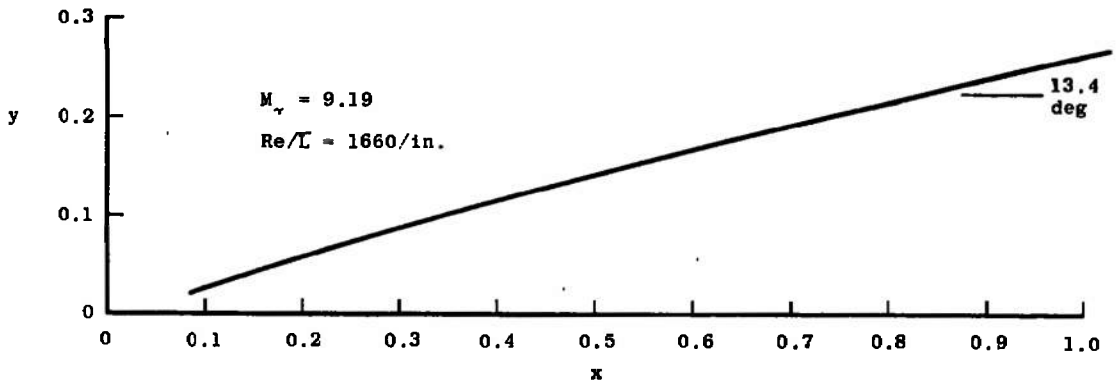

Fig. 11 Locus of Density Peaks

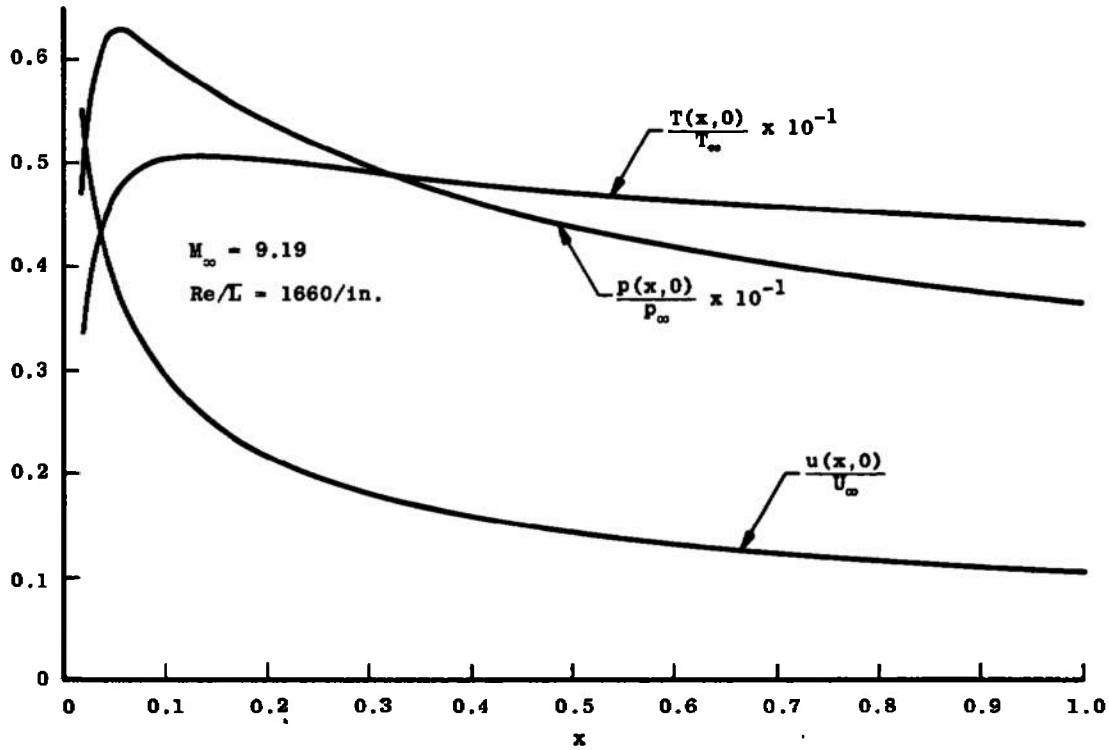

Fig. 12 Surface Pressure, Temperature, and Velocity Variation

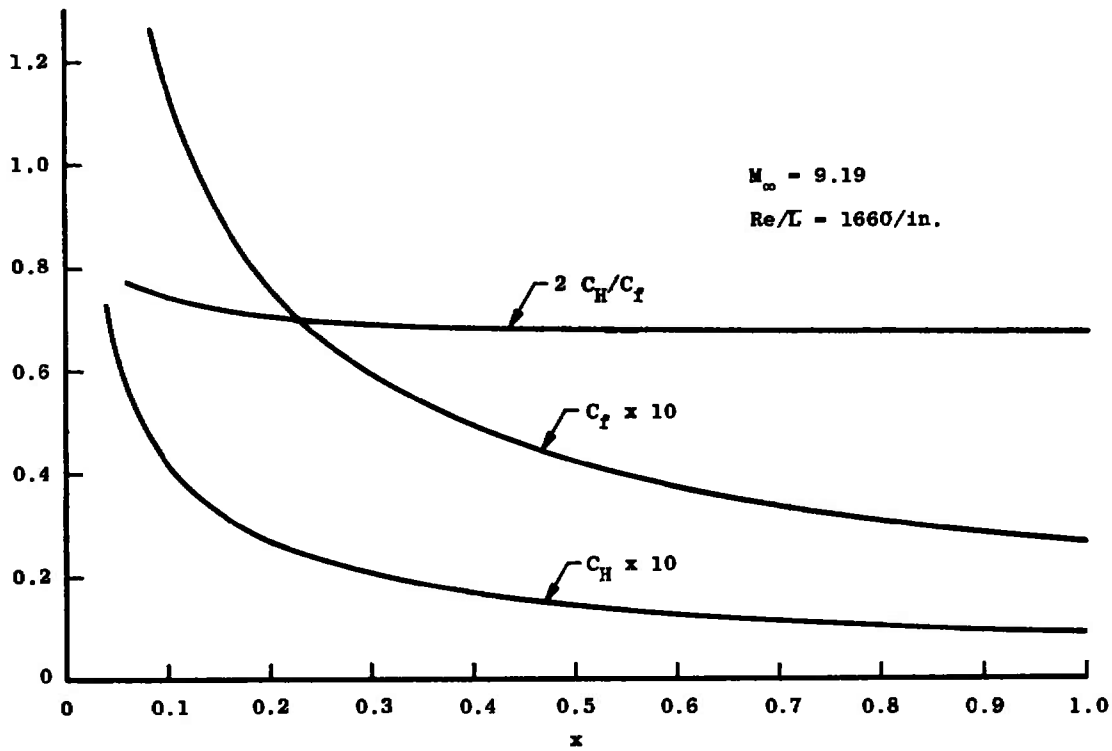

Fig. 13 Variation of Skin-Friction and Heat-Transfer Coefficients

Figures 14 through 17 show velocity, temperature, pressure, and density profiles on a flat plate, a 10-deg wedge, and a 10-deg cone under identical free-stream conditions. The gas in these calculations is again nitrogen, and the free-stream conditions are tabulated below:

$M_\infty = 10.15$ $\quad \gamma = 1.4$

$p_\infty = 20\mu$Hg $\quad T_w = 300°K$

$T_\infty = 144°K$ $\quad Pr = 0.71$

$Re/L = 388/in.$

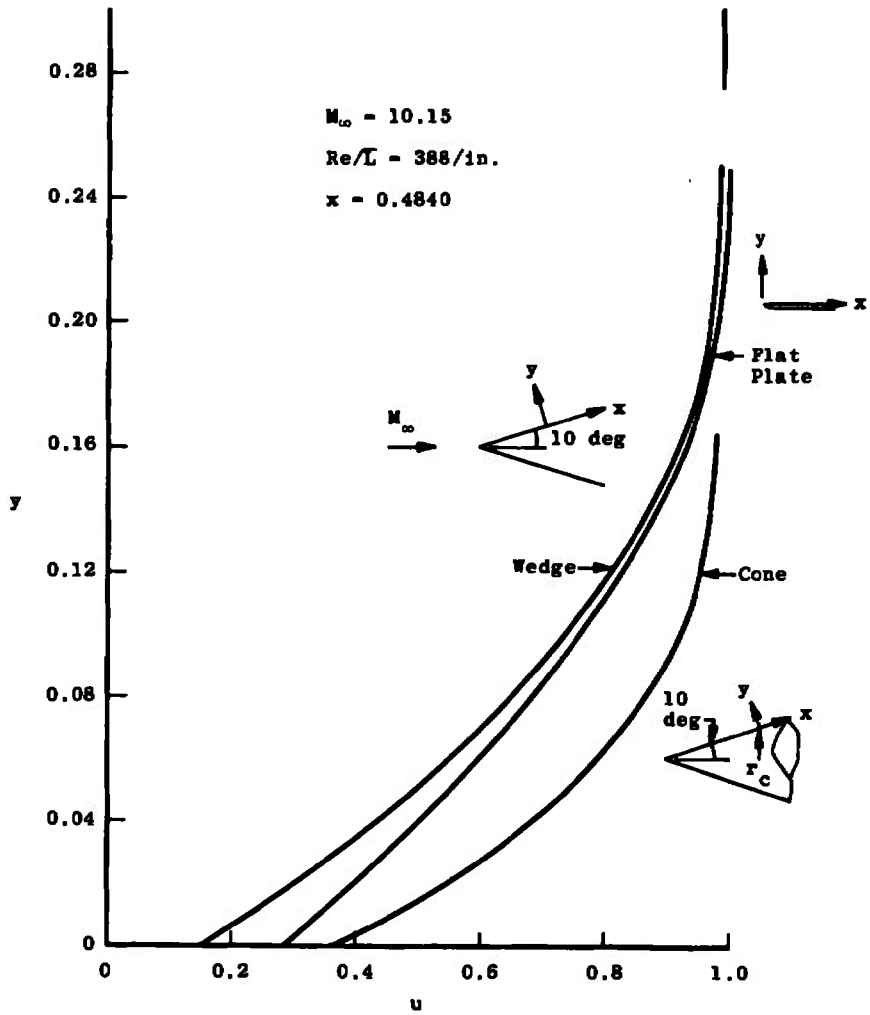

Fig. 14 Comparison of Velocity Profiles for Flat Plate, Wedge, and Cone

It is of interest first to compare the flat-plate profiles for this case with the higher-density conditions M_∞ = 9.19 and Re/L = 1660/in. shown in Figs. 6 through 9. Comparing the density profiles at x ≈ 0.8 shows that the center of the shock as indicated by the density peak is approximately the same for both cases but that the shock structure is not nearly so sharply defined for the lower-density case. For this low Reynolds number flow the shock is still very diffuse and buried within the viscous boundary-layer region.

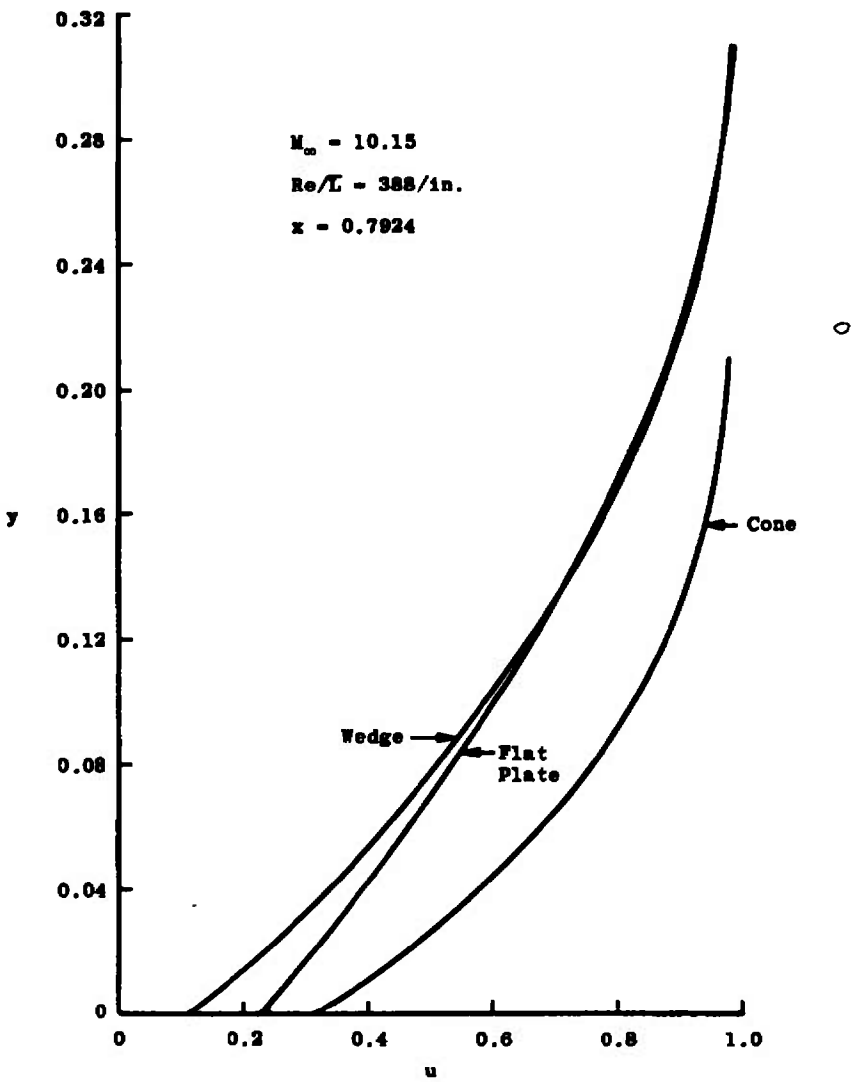

Fig. 14 Concluded

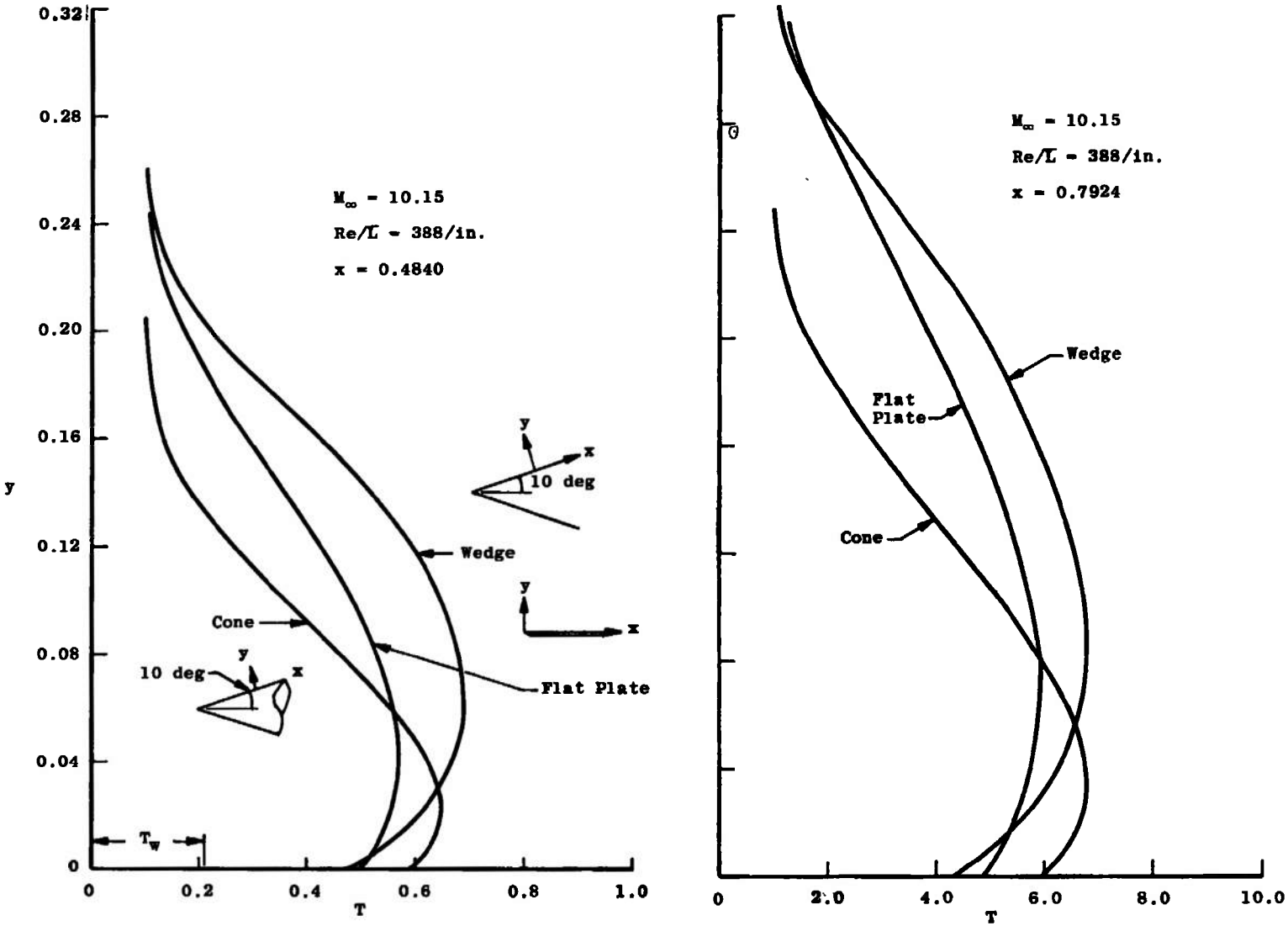

Fig. 15 Comparison of Temperature Profiles for Flat Plate, Wedge, and Cone

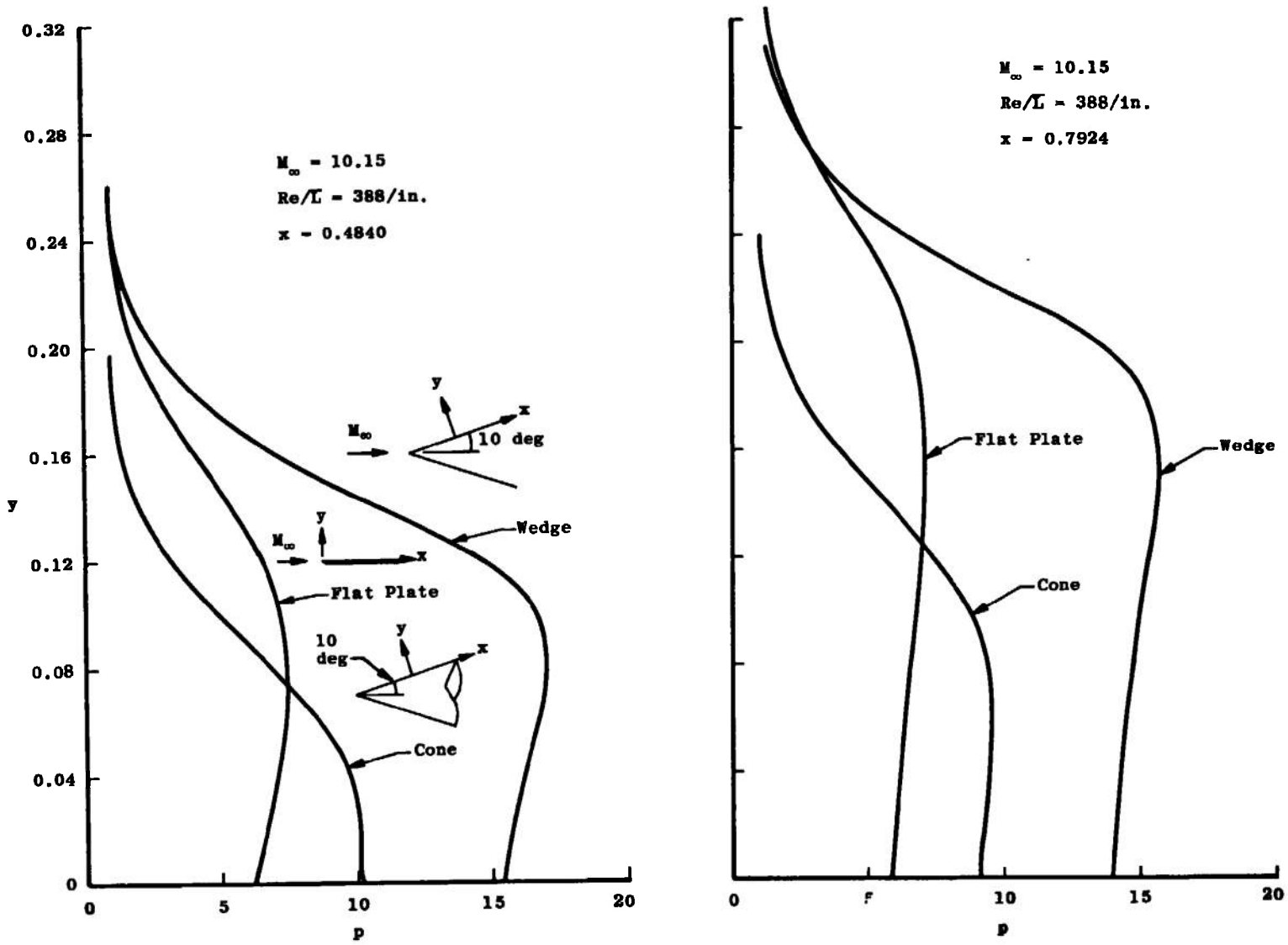

Fig. 16 Comparison of Pressure Profiles for Flat Plate, Wedge, and Cone

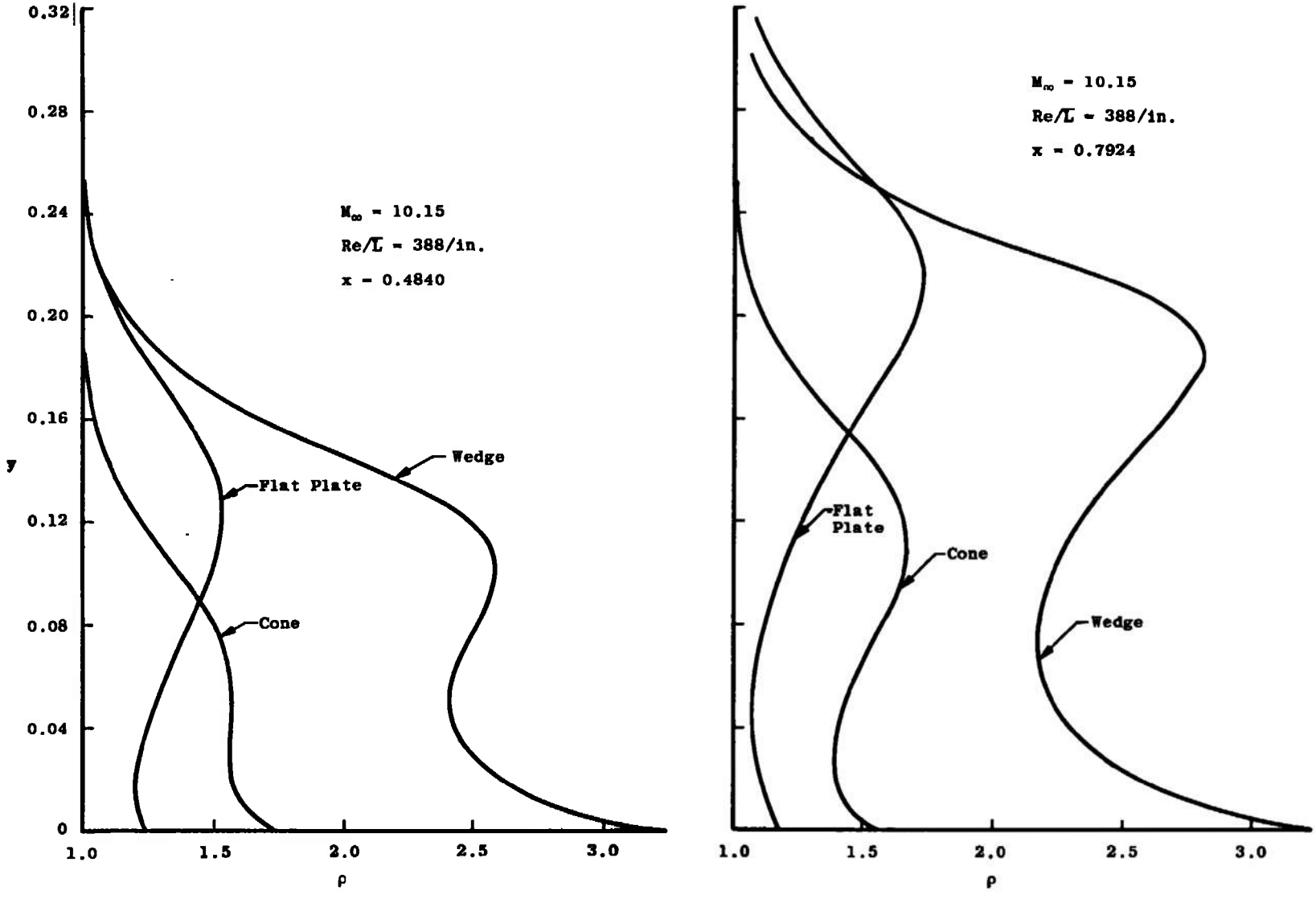

Fig. 17 Comparison of Density Profiles for Flat Plate, Wedge, and Cone

These figures also show that shock structure on the 10-deg wedge is much stronger and develops much more rapidly than on the flat plate. The pressure level is also much higher on the wedge, resulting in a higher density and a lower slip velocity. While the thickness of the shock layer is approximately the same for the wedge flow and the flat plate, the thickness for the cone is considerably reduced. This is typical of conical flows and is a result of the three-dimensional character of the flow field.

4.2 COMPARISON WITH DATA

A comparison of the results of the theoretical calculation method presented in this report with experimental data from several sources was carried out. These comparisons are shown in Figs. 18 through 27.

Figures 18 and 19 are comparisons of computed surface pressure with pressure data collected by Becker and Boylan (Ref. 16) in Tunnel L. Two calculated curves are shown in each of these figures, one labeled "pressure slip" and the other labeled "no pressure slip." The curve labeled "no pressure slip" gives simply the gas pressure evaluated at y = 0. The "pressure slip" curves on these two figures have been adjusted according to the correction given by Patterson (Ref. 17), as follows:

$$\frac{\bar{p}(0)}{\bar{p}_w} = 1 - \frac{5}{6}\left[\frac{\bar{\ell}}{\bar{c}}\left(\frac{\partial \bar{u}}{\partial \bar{x}} - 2\frac{\partial \bar{v}}{\partial \bar{y}}\right)\right]_{v=0} + \frac{15}{16}\left(\frac{\bar{\ell}}{\bar{T}}\frac{\partial \bar{T}}{\partial y}\right)_{y=0} \qquad (50)$$

where

$\bar{p}(0)$ = gas pressure at y = 0

$\bar{p}_w$ = wall pressure

$\bar{c} = \frac{8}{\pi} R\bar{T}$. average molecular speed

$\bar{\ell}$ = molecular mean free path

The above correction was obtained by assuming the diffuse reflection of gas molecules impinging on the wall. The reflected molecules are assumed to be in equilibrium at the temperature of the wall. By considering the transfer of tangential momentum and translational energy at the gas/solid interface, Patterson derived the velocity slip and temperature jump boundary conditions corresponding to Eqs. (7) and (8)

with the coefficients σ and α both equal to 1. A similar treatment of the normal component of momentum across the interface yields the relation between p(0) and p_w given in Eq. (50). This correction is therefore consistent with the slip boundary conditions applied to this study. The pressure correction is applied after the solution is obtained and does not affect the calculation of quantities in the flow field.

Written in dimensionless form in terms of (ξ, η) variables, Eq. (50) becomes

$$\frac{p(0)}{p_w} = 1 - \frac{5}{6}\sqrt{\frac{\gamma\pi}{8}}\, M_\infty \left[\frac{\bar{\ell}}{L}\left(\frac{\partial u}{\partial \xi} - \frac{2}{\rho}\frac{\partial v}{\partial \eta}\right)\right]_{\eta=0} + \frac{15}{16}\left(\frac{\bar{\ell}}{L}\frac{1}{\rho T}\frac{\partial T}{\partial \eta}\right)_{\eta=0}$$

As can be seen from Figs. 18 and 19, the pressure slip correction is a sizable fraction of the calculated surface pressure values. These figures also show that the corrected values agree much better with the pressure data obtained by Becker and Boylan than do the uncorrected values. To the author's knowledge this is the first time that the significance of the pressure slip correction for low-density hypersonic flow has been demonstrated.

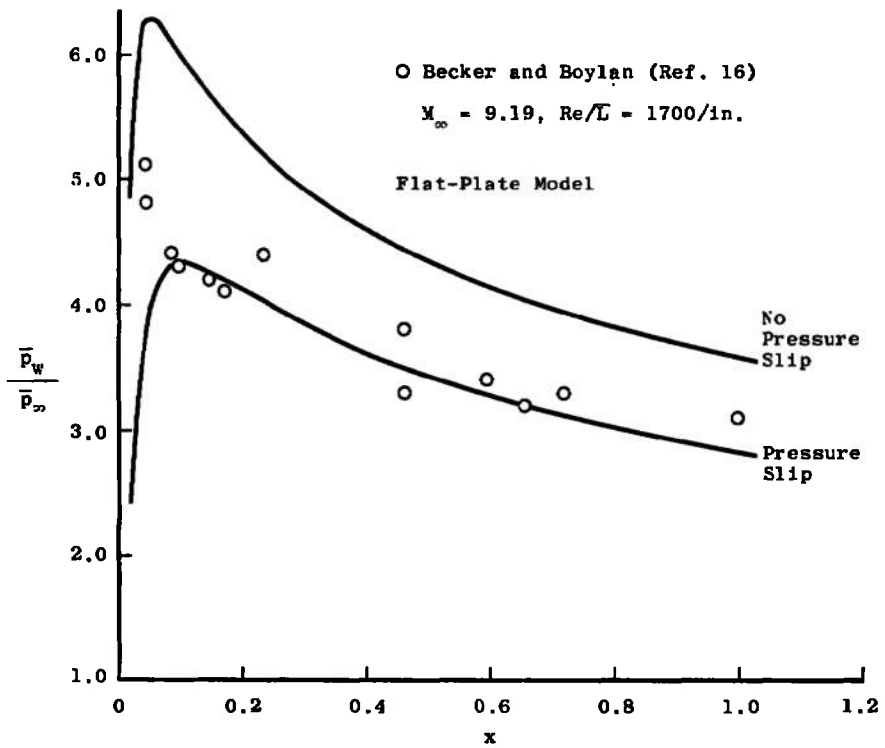

Fig. 18 Comparison of Calculated Surface Pressure with Experimental Data: High Reynolds Number

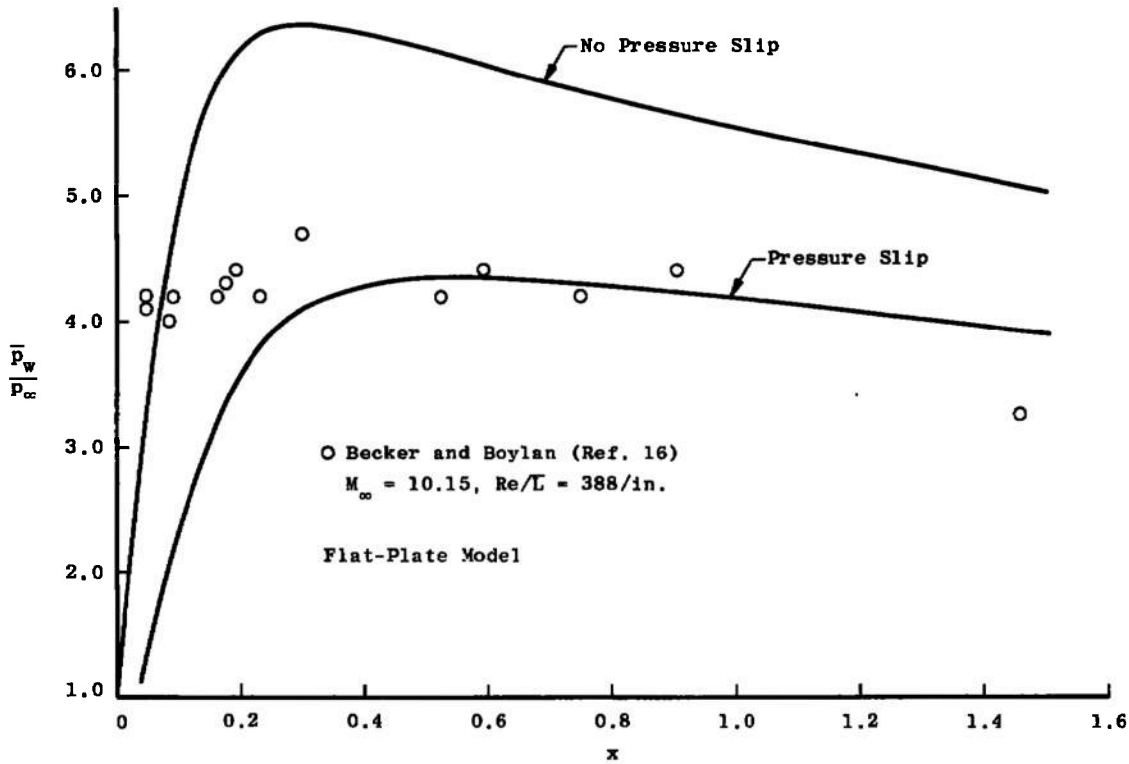

Fig. 19 Comparison of Calculated Surface Pressure with Experimental Data: Low Reynolds Number

Figures 20 and 21 show a comparison of calculated heat-transfer rate with experimental data obtained in Tunnel L by Boylan (Ref. 18). The heat-transfer rate was computed from the formula

$$\dot{q} = -\left(\bar{k}\,\frac{\partial \bar{T}}{\partial \bar{y}} + \bar{\mu}\,\bar{u}\,\frac{\partial \bar{u}}{\partial \bar{y}}\right)_{\bar{y}=0}$$

including the sliding friction term given by Maslen (Ref. 19). Note that Fig. 20 is for a flat plate at zero angle of attack and Fig. 21 is for a plate inclined at -10 deg to the flow stream. In all cases the agreement between calculated values and the experimental data is satisfactory.

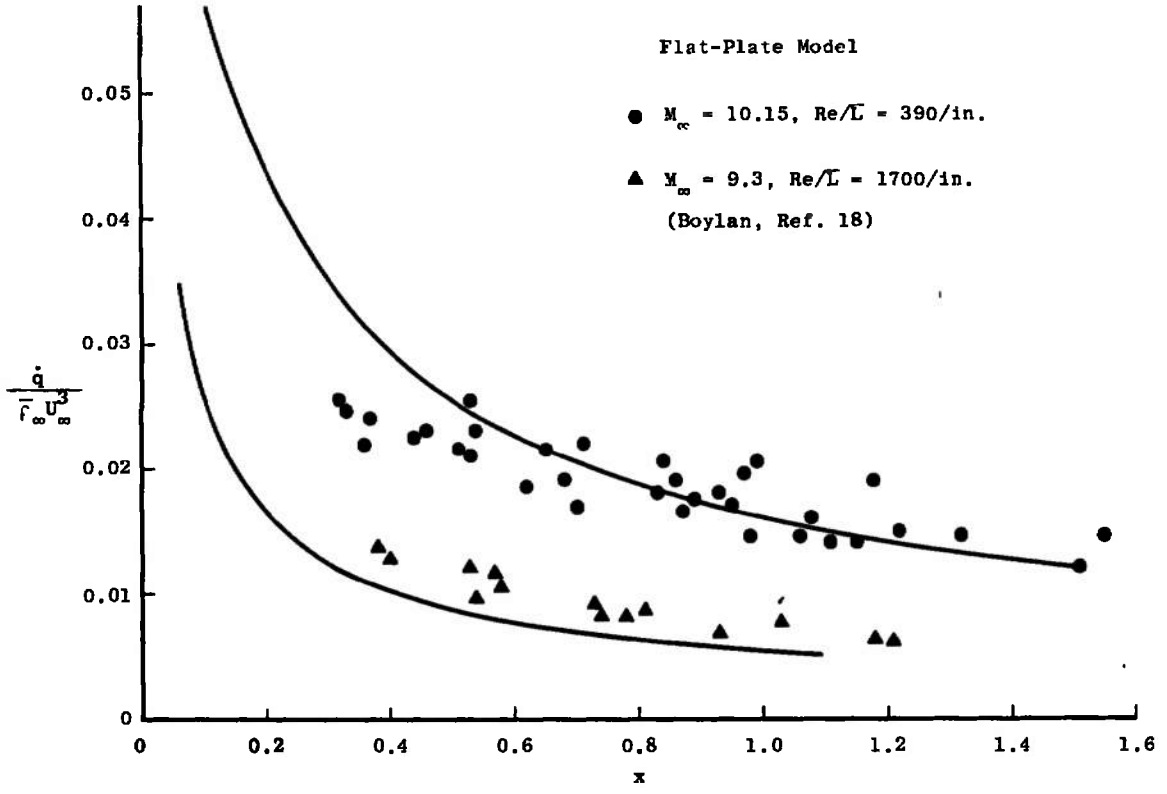

Fig. 20 Comparison of Calculated Heat-Transfer Rate with Experimental Data: High Reynolds Number

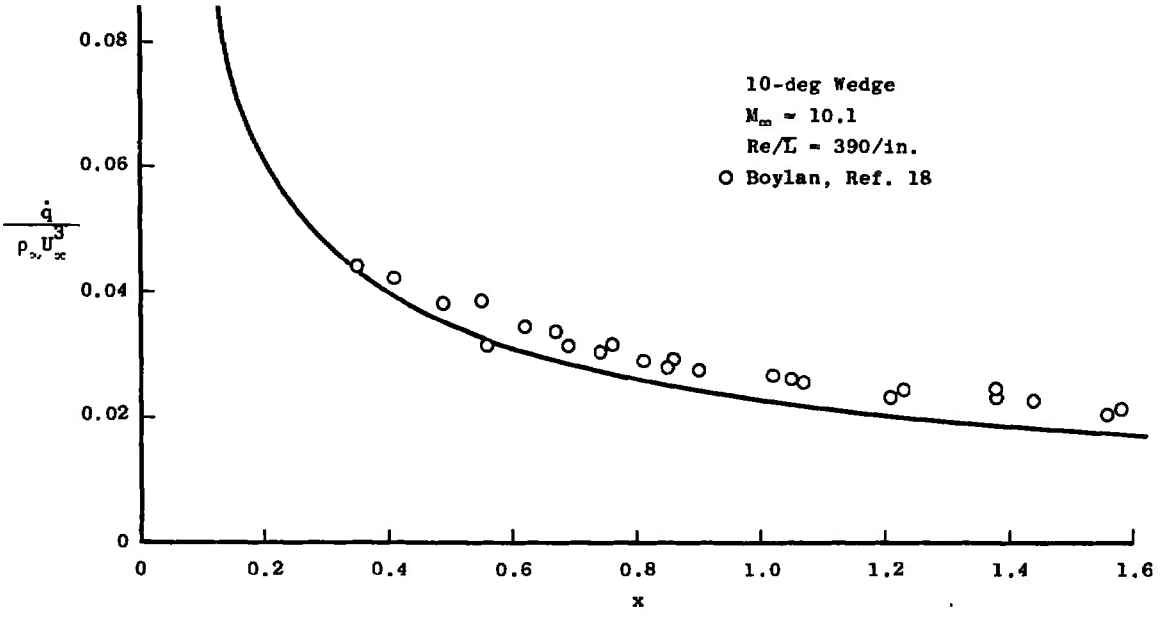

Fig. 21 Comparison of Calculated Heat-Transfer Rate with Experimental Data: Low Reynolds Number

Figure 22 shows the location of the center of shock structure as determined by the maximum pitot pressure in the shock layer. The agreement between the prediction of the present theory and the experimental data of Becker and Boylan (Ref. 16) is seen to be excellent.

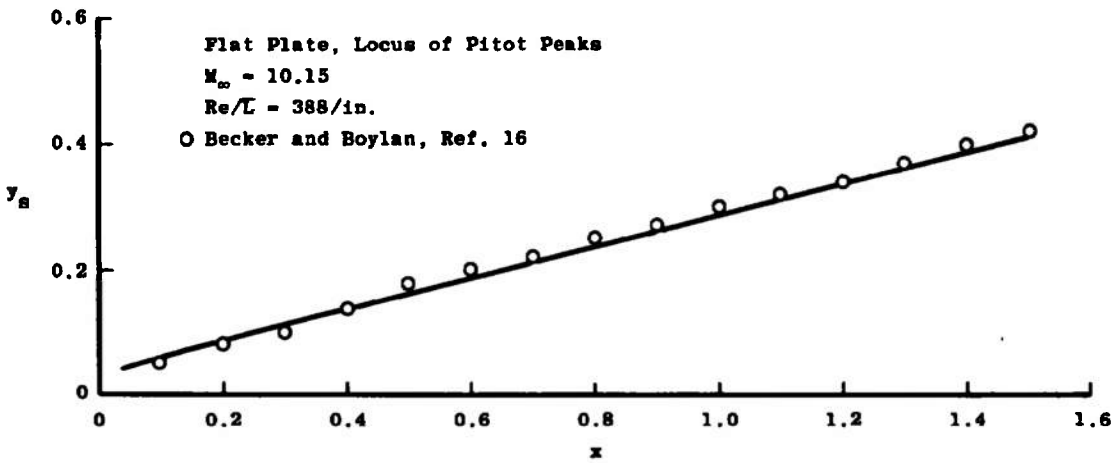

Fig. 22 Comparison of Calculated Shock Location with Experimental Data

Figure 23 shows a comparison of computed total pressure profiles at three stations with data of Ref. 16. The level of the pitot pressure peak as well as its height is predicted very well. These profiles show, however, that the computed thickness of the shock structure is considerably smaller than that which actually occurs. The computed total pressure profiles for argon shown in Fig. 24 likewise exhibit a thinner shock structure than the experimental profiles measured by Becker (Ref. 20). The location and level of the total pressure peaks do not agree as well with the data for this case. This calculation was made for the monatomic gas to determine whether rotational nonequilibrium effects could be responsible for the thickened shock structure. The results of the comparison would appear to deny this explanation. This underprediction of the shock structure thickness was also obtained by Cheng et al. (Ref. 8) and appears to be characteristic of shock models based on the Navier-Stokes equations.

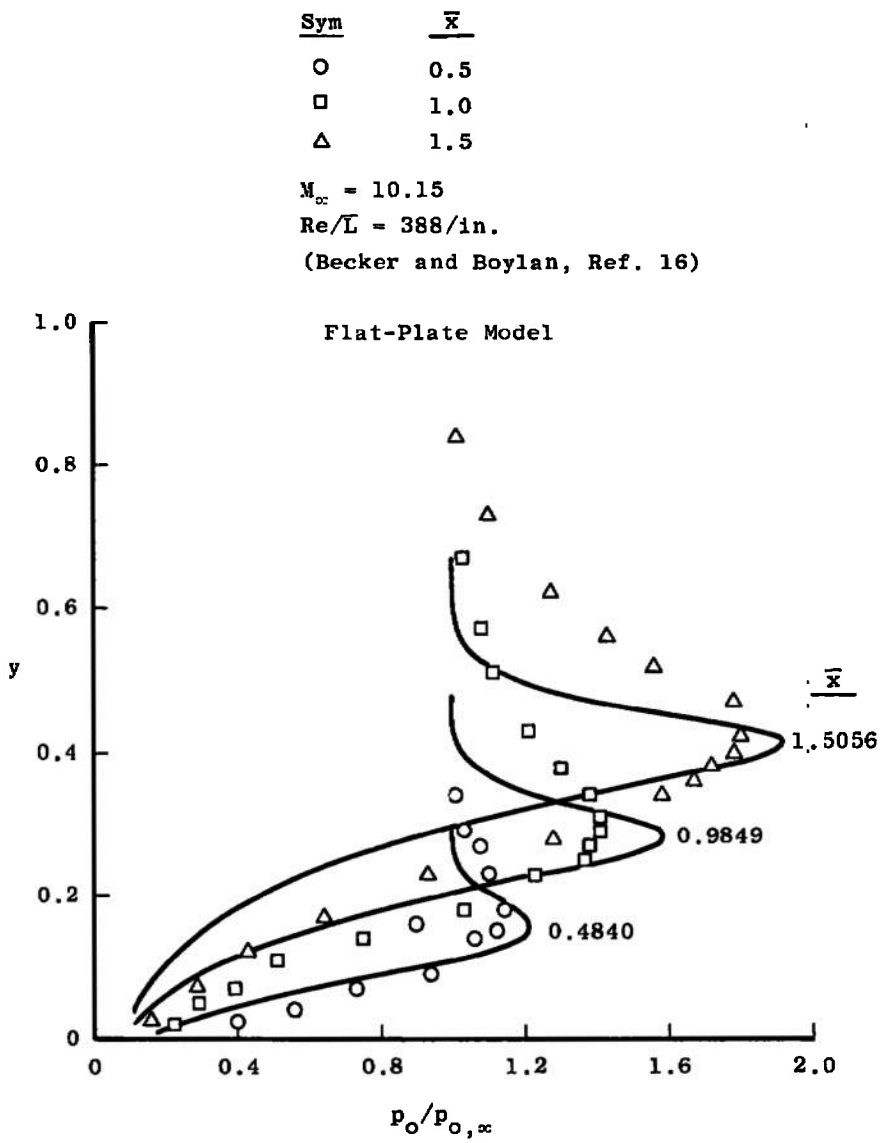

Fig. 23 Comparison of Calculated Total Pressure Profiles with Experimental Data for Nitrogen

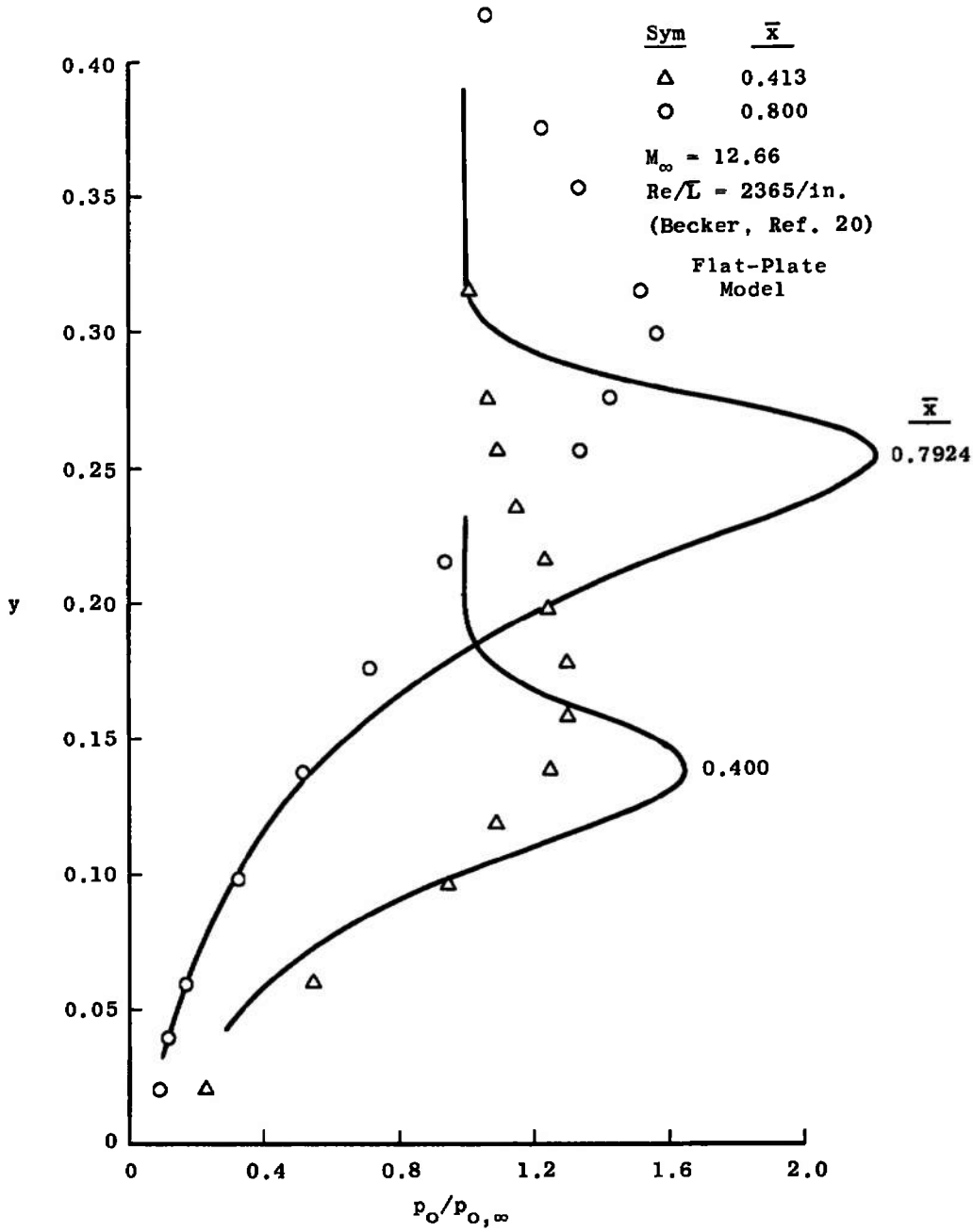

Fig. 24 Comparison of Calculated Total Pressure Profiles with Experimental Data for Argon

Figure 25 shows a comparison of computed density profiles with some experimental profiles obtained by McCrosky (Ref. 21) in nitrogen flow at very high Mach number. The location and level of the density peak are well predicted by the present calculation procedure. Also shown in Fig. 25 as solid symbols are some points taken from density profiles computed by Cheng et al. (Ref. 8) under identical conditions. Their results are very close to the profiles obtained in the present study, except near the center of the shock structure. In this region, Cheng et al. obtained a density level somewhat higher than that calculated in this investigation or shown in the data of McCrosky. At x = 2 in. Cheng's profiles exhibit the spurious kink in the shock region; therefore, this peak is not plotted in Fig. 25. The better agreement obtained in the present study is attributed to the more accurate set of equations used and the better finite-difference description in the shock region due to the stretching transformation (Eq. 18).

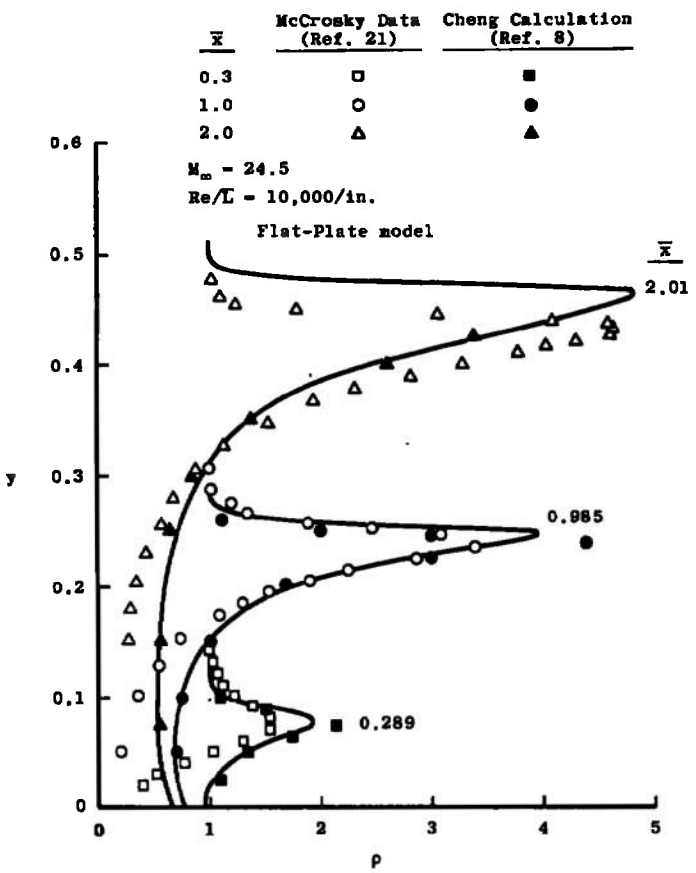

Fig. 25 Comparison of Calculated Density Profiles with Experimental Data for Nitrogen

Figures 26 and 27 show a correlation of surface pressure and heat-transfer data for flat plates from several sources. A replot of some of the data from the VKF tunnels is included in these figures. The surface pressure and heat-transfer coefficients are plotted in terms of the hypersonic interaction parameter $\overline{V}_{x,\infty} = \frac{M_\infty \sqrt{\overline{C}}}{\sqrt{Re_x}}$. Note that $\overline{V}_{x,\infty} \propto x^{-1/2}$ so that large values of $\overline{V}_{x,\infty}$ occur near the leading edge of the plate. The hypersonic parameter $\overline{\chi}$ is defined as

$$\overline{\chi} = \frac{M_\infty^3 \sqrt{\overline{C}}}{\sqrt{Re_x}} = \overline{V}_{x,\infty} M_\infty^2$$

where C is the Chapman-Rubesin constant.

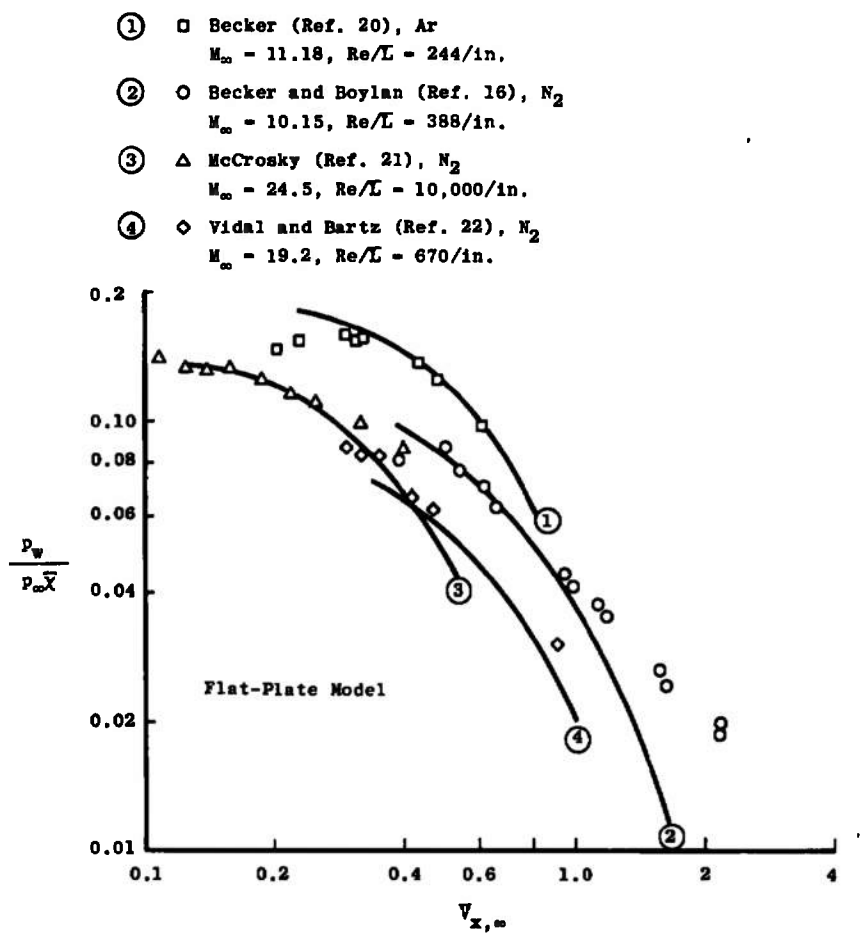

Fig. 26 Comparison of Calculated Surface Pressure Parameter with Experimental Data from Several Sources

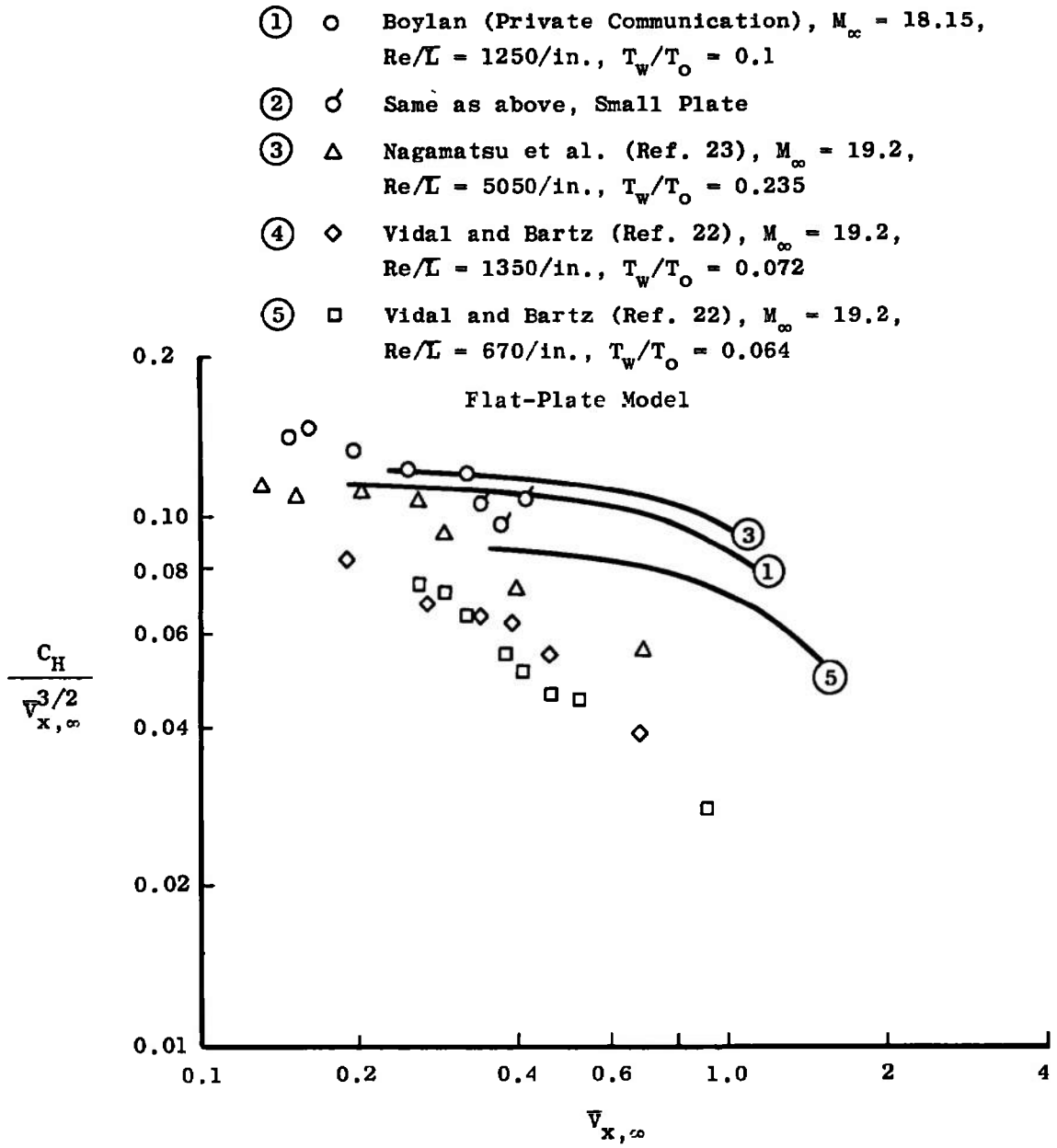

Fig. 27 Comparison of Calculated Heat-Transfer Coefficient with Experimental Data from Several Sources

The conditions used to calculate the solid curves in these two figures are designated by the numbered label and are given by the like-numbered experimental conditions in the figure legends.

The agreement between the computed surface pressure and the experimental data shown in Fig. 26 is considered to be reasonably good. The computed values, however, tend to be somewhat low near the leading edge of the plate. The surface pressure distributions shown in Figs. 18 and 19 suggest that this difficulty may have been caused by the uniform initial profiles that were used to start all calculation. However, the calculations for M_∞ = 10.15, Re/L = 388/in. were repeated using different initial velocity and temperature profiles, and the surface pressure distribution was not significantly altered.

The comparison with heat-transfer data for flat plates shown in Fig. 27 is less satisfactory. In particular, the data of Vidal and Bartz (Ref. 22) is far below the corresponding calculations. In view of the good agreement with the heat-transfer data taken in Tunnel L as shown in Figs. 20 and 21, the author considers this to be an indication that the data reported in Ref. 22 may be somewhat low.

SECTION V
SUMMARY AND CONCLUSIONS

An analytical investigation has been carried out and a numerical procedure developed for calculating fully viscous shock-layer flow near the leading edge of two-dimensional and axisymmetric slender bodies under low-density hypersonic conditions. The particular geometries considered were two-dimensional flat plates at zero and negative angles of attack and axisymmetric cones at zero angle of attack. The calculation method is based on numerical integration of the continuum fluid mechanical equations of motion using an implicit finite-difference marching technique. The mathematical model used in this investigation represents an improvement over previously published continuum studies in that a more complete and accurate set of governing equations is employed. Standard slip and temperature jump boundary conditions are employed at the wall, and the shock structure is determined as part of the resulting solution. In order to obtain adequate resolution in the shock wave region, the normal coordinate is stretched by using a Howarth transformation.

The results of the calculations show quite clearly (1) the development of a merged flow regime where the shock is buried in the viscous region and (2) the transition to the strong interaction regime where a well-defined shock structure exists. Near the leading edge there is a pronounced pressure variation throughout the shock layer, whereas further downstream there is a substantial portion of the flow field where $\frac{\partial p}{\partial y} = 0$.

The results of the numerical calculations have been compared with experimental data from a number of sources, and qualitative agreement with surface-pressure and heat-transfer data as well as with profile data was obtained for all cases tested. The quantitative agreement of the surface-pressure data was markedly improved by the application of a pressure slip correction derived by Patterson (Ref. 17). A comparison of the results of the present theory with experimental data obtained on flat plate and wedges in Tunnel L reveals very good agreement.

REFERENCES

1. Pan, Y. S. and Probstein, R. F. "Rarefied Flow Transition at a Leading Edge." Publication No. 64-8, Fluid Mechanics Laboratory, Massachusetts Institute of Technology, October 1964.

2. Shorenstein, M. L. and Probstein, R. F. "The Hypersonic Leading-Edge Problem." AIAA Paper No. 68-4, January 1968.

3. Oguchi, H. "Shock Wave and Viscous Layer Structure in a Rarefied Hypersonic Flow Near the Leading Edge of a Sharp Flat Plate." Report of Institute of Space and Aeronautical Science, University of Tokyo. Vol. 32, No. 418, December 1967.

4. Chow, W. L. "Hypersonic Rarefied Flow Past the Sharp Leading Edge of a Flat Plate." AIAA J., Vol. 5, No. 9 (September 1967), pp. 1549-57.

5. Rudman, S. and Rubin, S. G. "Hypersonic Viscous Flow over Slender Bodies Having Sharp Leading Edges." PIBAL Report No. 1018, Polytechnic Institute of Brooklyn, Farmingdale, N. Y., May 1967.

6. Rudman, S. and Rubin, S. G. "Hypersonic Viscous Flow Over Slender Bodies with Sharp Leading Edges." AIAA J., Vol. 6, No. 10 (October 1968), pp. 1883-1889.

7. Rubin, S. G. et al. "Hypersonic Interactions near Sharp Leading Edges." AIAA J., Vol. 7, No. 9 (September 1969), pp. 1744-1751.

8. Cheng, H. K. et al. "The Viscous Hypersonic Slender Body Problem: A Numerical Approach Based on a System of Composite Equations." Memorandum RM-6193-PR, The Rand Corporation, May 1970.

9. Token, K. H. "Viscous Hypersonic Flow in Divergent, Slender Axisymmetric Nozzles." Ph.D. Dissertation, The University of Tennessee Space Institute, December 1970.

10. Kot, S. C. and Turcotte, D. L. "Beam-Continuum Model for Hypersonic Flow over a Flat Plate." AIAA J., Vol. 10, No. 3 (March 1972), pp. 291-295.

11. Lagerstrom, P. A. "Laminar Flow Theory." Section B, Theory of Laminar Flows, ed. F. K. Moore. Princeton, N. J., Princeton University Press, 1964.

12. Schaaf, S. A. and Chambré, P. L. Flow of Rarefied Gases. Princeton, N. J., Princeton University Press, 1961.

13. Blottner, F. G. "Finite Difference Methods of Solution of the Boundary-Layer Equations." AIAA J., Vol. 8, No. 2 (February 1970), pp. 193-205.

14. Davis, R. T. "Numerical Solution of the Hypersonic Viscous Shock-Layer Equations." AIAA J., Vol. 8, No. 5 (May 1970), pp. 843-851.

15. Richtmyer, R. D. and Morton, K. W. Difference Methods for Initial-Value Problems. 2d Ed. New York, John Wiley and Sons, Inc., 1967.

16. Becker, M. and Boylan, D. E. "Flow Field and Surface Pressure Measurements in the Fully Merged and Transition Flow Regimes on a Cooled Sharp Flat Plate." AEDC-TR-66-111 (AD638804), September 1966.

17. Patterson, G. N. Molecular Flow of Gases. New York, John Wiley and Sons, Inc., 1956.

18. Boylan, D. E. "Measurement of Convective Heat-Transfer Rate to a Cooled Sharp Flat Plate in Hypersonic Merged Flow." ASME Paper No. 69-WA/HT-21, December 1969.

19. Maslen, S. H. "On Heat Transfer in Slip Flow." J. Aeronautical Sciences. Vol. 25, No. 6 (June 1958), pp. 400-401.

20. Becker, M. "Flat Plate Flow Field and Surface Pressure Measurements from Merged Layer into Transition Regime." Rarefied Gas Dynamics, Supplement 5, Vol. 1, 1969, pp. 515-528.

21. McCrosky, William J. "An Experimental Model for the Sharp Leading Edge Problem in Rarefied Hypersonic Flow." ARL 66-0101, Aerospace Research Laboratories, Wright-Patterson A. F. B., Ohio, June 1966.

22. Vidal, R. J. and Bartz, J. A. "Surface Measurements on Sharp Flat Plates and Wedges in Low Density Hypersonic Flow." CAL Report No. AF 2041-A-2, Cornell Aeronautical Laboratory, February 1968.

23. Nagamatsu, H. T., Pettit, W. T., and Sheer, R. E., Jr. "Heat Transfer on a Flat Plate in Continuum to Rarefied Hypersonic Flows at Mach Numbers of 19.2 and 25.4." NASA CR-1692, November 1970.

UNCLASSIFIED

Security Classification

DOCUMENT CONTROL DATA - R & D

(Security classification of title, body of abstract and indexing annotation must be entered when the overall report is classified)

1 ORIGINATING ACTIVITY (Corporate author) Arnold Engineering Development Center Arnold Air Force Station, Tennessee 37389	2a. REPORT SECURITY CLASSIFICATION UNCLASSIFIED 2b GROUP N/A

3 REPORT TITLE

AN ANALYTICAL INVESTIGATION OF VISCOUS SHOCK-LAYER FLOW NEAR THE LEADING EDGE OF SLENDER BODIES UNDER LOW-DENSITY HYPERSONIC CONDITIONS

4 DESCRIPTIVE NOTES (Type of report and inclusive dates)

Final Report -- July 1969 to July 1972

5 AUTHOR(S) (First name, middle initial, last name)

J. R. Maus, ARO, Inc.

6 REPORT DATE June 1973	7a TOTAL NO OF PAGES 55	7b NO OF REFS 23
8a CONTRACT OR GRANT NO b PROJECT NO c. Program Element 65802F d	9a. ORIGINATOR'S REPORT NUMBER(S) AEDC-TR-73-102 9b OTHER REPORT NO(S) (Any other numbers that may be assigned this report) ARO-VKF-TR-73-26	

10 DISTRIBUTION STATEMENT

Approved for public release; distribution unlimited.

11 SUPPLEMENTARY NOTES Available in DDC.	12 SPONSORING MILITARY ACTIVITY Arnold Engineering Development Center, Air Force Systems Command, Arnold AF Station, TN 37389

13 ABSTRACT

An analytical investigation and a numerical procedure are presented for calculating the fully viscous shock-layer flow near the sharp leading edge of both two-dimensional and axisymmetric slender bodies under hypersonic low-density flow conditions. The calculation method is based on numerical integration of the governing continuum fluid mechanical equations of motion using an implicit finite-difference technique in conjunction with wall slip boundary conditions; the shock structure is determined as part of the resulting solution. The mathematical model used in the present investigation represents a considerable improvement over previously published continuum studies in that a more complete and accurate set of governing equations and boundary conditions is employed. The results of the numerical calculations have been compared with previous flat-plate test results taken in the von Kármán Facility Low Density Hypersonic Wind Tunnel (L) by Becker and Boylan; in general, good to excellent agreement between the present theory and experiment is revealed.

DD FORM 1 NOV 65 1473

UNCLASSIFIED

Security Classification

14 KEY WORDS	LINK A		LINK B		LINK C	
	ROLE	WT	ROLE	WT	ROLE	WT
shock waves						
hypersonic flow						
leading edges						
boundary layer						
mathematical model						
continuum mechanics						

AFSC
Arnold AFS Tenn